Catalysis Science & Technology

ROYAL SOCIETY OF CHEMISTRY

REVIEW

View Article Online
View Journal | View Issue



Cite this: *Catal. Sci. Technol.*, 2024, **14**, 6443

# Innovations in nanocomposite photocatalysts for $CO_2$ to $CH_3OH$ conversion

Shuang Deng,[a] Nannan Wang, *[a] Yanqiu Zhu [b] and Kunyapat Thummavichai *[c]

Nowadays, the excessive use of fossil fuels has led to a global energy shortage and exacerbated the greenhouse effect. One of the main contributors to the greenhouse effect is the excessive emission of carbon dioxide ($CO_2$). Therefore, to achieve sustainable development and harmonious symbiosis between humans and nature, reducing $CO_2$ emission has become a global concern. Converting $CO_2$ into value-added products can effectively address this issue. At present, the photocatalytic reduction of $CO_2$ using synthetic nanocomposites is a common method. Among the products of photocatalytic $CO_2$ reduction, methanol ($CH_3OH$) shows promise as a new clean fuel and basic chemical raw material, with potential to reduce energy consumption. This paper reviews the research progress of photocatalytic reduction of $CO_2$ to $CH_3OH$ in recent years. The difficulties and challenges in the photocatalytic process, along with potential solutions, are briefly discussed. Finally, the future prospects of this research are outlined.

Received 2nd July 2024,
Accepted 24th August 2024

DOI: 10.1039/d4cy00822g

rsc.li/catalysis



## 1. Introduction

In the course of human development, science and technology have not only brought convenience to human life, but also enriched the living environment. However, for the entire ecological environment, science and technology act as a "double-edged sword", presenting a series of negative effects. During the rapid pace of global industrialization, the excessive use of fossil fuels has led to significant greenhouse gas emissions, resulting in the greenhouse effect and global climate warming. Carbon dioxide ($CO_2$) is one of the most common greenhouse gases. Under normal circumstances, $CO_2$ is absorbed by plants through photosynthesis to produce oxygen, essential for human survival. However, due to the indiscriminate exploitation of forest resources, $CO_2$ emissions have increased year by year, failing to meet the requirements for sustainable human development. In order to solve this problem, the most effective approach is to convert $CO_2$ into chemical raw materials needed for human development, thereby achieving its recycling. Through continuous exploration, researchers have identified several effective methods to reduce the concentration of $CO_2$ in the atmosphere, such as thermal–chemical methods, biological methods, electrochemical methods and photocatalysis methods.[1] Simulating plant photosynthesis to convert $CO_2$ into hydrocarbons through photocatalysis is considered a more viable approach for achieving clean energy and sustainable development. Compared to other methods, this method is not only simple and convenient, but also avoids secondary pollution. Additionally, the final product can be used as green renewable energy, thereby alleviating the global energy shortage problem.

Because the C=O bond energy of $CO_2$ is high, the activation energy required to disconnect this bond is substantial, posing a significant challenge to the photocatalytic $CO_2$ reduction process. To design and synthesize efficient photocatalysts, researchers commonly use nanocomposites for photocatalytic $CO_2$ reduction. The final products are mainly divided into two categories: C1 products and C2 and C2+ products. Among them, C1 products include CO, $CH_4$, $CH_3OH$, HCOOH, *etc.* C2 and C2+ products include $C_2H_4$, $C_2H_6$, $C_3H_6$, $C_2H_5OH$, *etc.*[2] Methanol ($CH_3OH$) is the simplest saturated monohydric alcohol. It is not only an important basic organic chemical raw material but also a new type of clean energy fuel. $CH_3OH$ is widely used for the synthesis of various organic compounds such as aldehydes, olefins, esters, *etc.* Additionally, it can be incorporated into gasoline as an alternative fuel and used as a fuel cell raw material. Currently, the industry primarily synthesizes methanol through pressurized catalytic hydrogenation of carbon monoxide and carbon dioxide. Although this technology is relatively mature, it involves a cumbersome

[a] *State Key Laboratory of Featured Metal Materials and Life-cycle Safety for Composite Structures, School of Resources, Environment and Materials, Guangxi University, Nanning, 530004, Guangxi, China. E-mail: wangnannan@gxu.edu.cn*
[b] *College of Engineering, Mathematics and Physical Sciences, University of Exeter, Exeter, EX4 4QF, UK*
[c] *Department of Mathematics, Physics and Electrical Engineering, Faculty of Engineering and Environment, Northumbria University, Newcastle-upon-Tyne, NE1 8ST, UK. E-mail: kunyapat.thummavichai@northumbria.ac.uk*

process flow and large energy consumption. In contrast, the photocatalytic reduction of $CO_2$ to $CH_3OH$ can be achieved at atmospheric pressure, offering a promising method for reducing energy consumption.

There have been reviews on the application of different photocatalysts in photocatalytic $CO_2$ reduction reactions. However, very few reviews focus on the preparation of $CH_3OH$. This paper aims to summarize the research on the photocatalytic reduction of $CO_2$ to $CH_3OH$ over the past five years, briefly discussing the reaction mechanism and the opportunities and challenges faced in this field.

## 2. Theoretical basis of photocatalytic reduction of $CO_2$ to $CH_3OH$

A catalyst is a substance that can accelerate a chemical reaction without itself participating in the reaction. Photocatalysts are a general term for chemicals that can play a catalytic role under the excitation of photons. Through continuous research, various types of photocatalysts have been developed, with semiconductor photocatalysts, particularly nanoscale titanium dioxide ($TiO_2$), being the most widely studied and applied. The principle of photocatalytic reactions can be explained by the band theory of semiconductors.[3] Unlike metals and insulators, semiconductors have a band gap between the valence band (VB) and the conduction band (CB). When they are illuminated by light with photon energy equal to or higher than the bandgap energy, electrons in the VB can be excited into the CB, creating corresponding holes in the VB and forming electron–hole pairs. The photocatalytic reaction process in semiconductors can be simply described as follows: (i) semiconductors absorb light to form electron–hole pairs, which then (ii) migrate and recombine. These processes allow redox reactions to occur on the surface of semiconductors through the adsorption of reactants and the desorption of products.

Fig. 1 illustrates the photocatalytic process of semiconductors, where electron–hole pair recombination can occur either within the material or on its surface. So far, the biggest bottleneck in photocatalytic reactions is low photocatalytic efficiency, primarily due to the rapid recombination of photogenerated electrons and holes.[4] Improving energy conversion efficiency involved expanding the range of light absorption to achieve more efficient photocatalytic reactions. However, developing a photocatalyst with high light-trapping capacity and effective charge separation, as well as abundant $CO_2$ adsorption active sites, remains a significant challenge.[5]

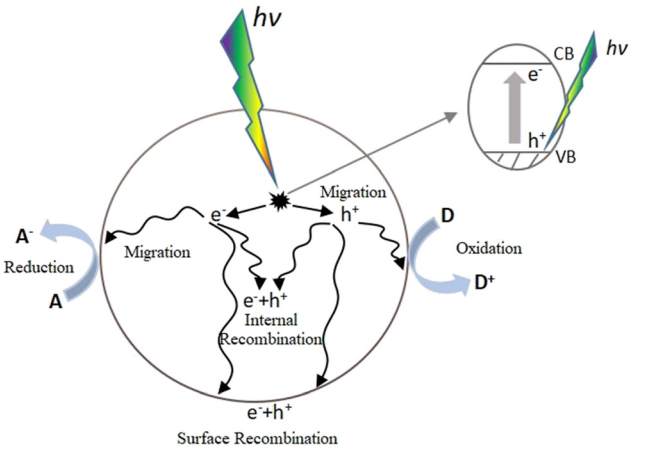


Fig. 1 Photocatalytic process of a semiconductor.

$CO_2$ is a symmetrical linear molecule, and because C═O (750 kJ $mol^{-1}$) has a much higher bond energy than C–C (336 kJ $mol^{-1}$), C–O (327 kJ $mol^{-1}$), and C–H (411 kJ $mol^{-1}$) bonds,[6] photocatalytic conversion of $CO_2$ usually requires a large amount of energy input to break C═O bonds. At the same time, $CO_2$ is optically inert under visible or ultraviolet radiation with a wavelength of 200–900 nm. Therefore, it is necessary to use a photocatalyst with a suitable band structure to enable photoexcitation and generate photoelectron–hole pairs to complete the reduction process of $CO_2$.[7] As the highest oxidation state of carbon, $CO_2$ can be reduced to a variety of products by obtaining different numbers of electrons and protons. The presence of by-products depletes valuable photogenerated electron–hole pairs, thereby reducing the formation of target products. Consequently, obtaining high yields of target products is a primary goal in photocatalytic $CO_2$ reduction reactions.[8] In the process of photocatalytic reduction of $CO_2$ to produce $CH_3OH$, the following chemical reaction formula is followed:[6]

$$CO_2 + 2H^+ + 2e^- \rightarrow CO + H_2O \quad E_1 = -0.53\ V \tag{1}$$

$$CO_2 + 6H^+ + 6e^- \rightarrow CH_3OH + H_2O \quad E_2 = -0.38\ V \tag{2}$$

The adsorption of $CO_2$ on the surface of the photocatalyst is a key step in facilitating the reaction. The adsorption structures of $CO_2$ on the surface of the photocatalyst mainly include oxygen, carbon and mixed coordination.[8] Different $CO_2$ adsorption structures will form different reaction pathways, resulting in different reaction products and intermediates. In the process of photocatalytic reduction of $CO_2$ to $CH_3OH$, there is often a competitive reaction with another product, $CH_4$. When $CO_2$ molecules obtain photogenerated electrons and $H^+$, they will be converted into ·COOH free radicals. Through a series of dehydration hydrogenation reactions, the product $CH_3OH$ can be obtained. If $CH_3OH$ is weakly bound to the photocatalyst surface, the desorption of $CH_3OH$ can be carried out more easily. However, if $CH_3OH$ binds strongly to the photocatalyst surface, it becomes difficult for $CH_3OH$ to be released on the surface of the photocatalyst, leading to further hydrodeoxidation reaction, and finally generating $CH_4$. This results in a decrease in the yield of $CH_3OH$. Therefore, synthesizing suitable photocatalysts and optimising the experimental conditions of photocatalysis are crucial strategies to improve the yield of $CH_3OH$.

 

## 3. Reduction of $CO_2$ to $CH_3OH$ by different photocatalytic systems

Photocatalysis is a technology that emerged in the 1970s, based on the redox ability of photocatalysts under light conditions to achieve the purification of pollutants, as well as the synthesis and transformation of the substances. The typical natural photocatalyst is chlorophyll, which promotes the conversion of $CO_2$ and $H_2O$ in the air into oxygen and carbohydrates during plant photosynthesis. Photocatalytic reduction of $CO_2$ aims to use light energy to convert $CO_2$ into high value-added chemicals or fuels by simulating this natural process. The photocatalytic systems used for photocatalytic reduction of $CO_2$ to $CH_3OH$ can be roughly divided into the following categories: layered bimetallic hydroxide-based (LDH) photocatalysts, graphite carbon nitride-based (g-$C_3N_4$) photocatalysts, graphene oxide-based (GO) photocatalysts, mixed metal compound photocatalysts, and single metal-doped photocatalysts. And from Fig. 2, it is easy to find that in the last 5 years, the most studies on mixed metal compound photocatalysts for photocatalytic reduction of $CO_2$ to $C_2H_5OH$ have been carried out.

### 3.1 Layered double hydroxide (LDH)-based photocatalyst

LDH is a two-dimensional (2D) nanomaterial with the general formula $[M^{2+}_{1-x}M^{3+}_x(OH)_2]^{q+}(X^{n-})_{q/n}{\cdot}yH_2O$, where typical $M^{2+}$ ions include $Mg^{2+}$, $Co^{2+}$, $Ni^{2+}$, $Cu^{2+}$, and $Zn^{2+}$, and $M^{3+}$ = $Al^{3+}$, $Cr^{3+}$, $Fe^{3+}$, $In^{3+}$, $Ga^{3+}$, *etc.*[9] In addition, $M^{1+}$ and $M^{4+}$ can also combine to form LDH, but currently, this is limited to combination of $Li^+$, $Ti^{4+}$, $Zr^{4+}$ and $Sn^{4+}$.[10] Photocatalytic materials with various properties can be obtained by adjusting the types and proportions of cations in the LDH layer. Furthermore, the photocatalytic performance can also be adjusted by changing the type of interlayer anion. Common interlayer anions are $CO_3^{2-}$, $OH^-$, $SO_4^{2-}$, $NO_3^-$, $F^-$, $Cl^-$, $Br^-$, *etc.*

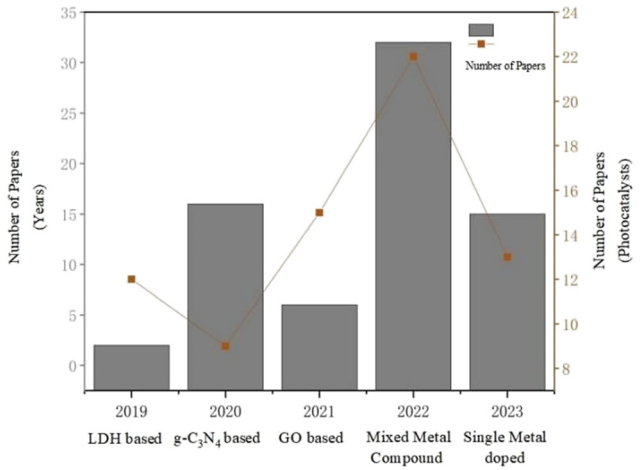


Fig. 2 The number of published papers on the photocatalytic reduction of $CO_2$ to $CH_3OH$ over different years, as well as the number of papers related to various types of photocatalysts in the past five years (data from Scholar Search).

As early as 2009, LDH was mainly used as a heterogeneous catalyst for base-catalyzed reactions or redox transformations due to its unique structure. However, in 2009, Silva *et al.*[11] considered the presence of two different metals in the LDH structure and the controllable ratio between them, hypothesizing that LDHs could function as "doped semiconductors". Silva *et al.* then prepared a series of LDHs with different Zn/metal atomic ratios (4 : 2 to 4 : 25) by the co-precipitation method, aiming to create an efficient photocatalyst for visible light oxygen production in water. The results showed that all the prepared materials exhibited good photocatalytic activity, with the Zn–Cr containing materials displaying the highest photocatalytic activity. Using monochromatic light, the apparent quantum yield of oxygen generation at 410 nm was as high as 60.9%.

In 2012, Teramura *et al.*[12] proposed that Mg–Al hydrotalcite anionic clays could catalyze the aldol reaction of carbonyl compounds in aqueous solutions due to the high water resistance of the surface basic groups. They suggested that if $CO_2$ is first adsorbed on the surface of the photocatalyst and then activated under light exposure, most LDH could act as a photocatalyst in water. Therefore, they synthesized LDH by co-precipitation and hydrothermal methods. The photocatalytic reduction of $CO_2$ was then carried out in a closed circulation system. The results showed that the surface base sites of LDH with high water resistance not only act as $CO_2$ adsorbents, but also as active sites for $CO_2$ activation under light irradiation. This confirms the potential for photocatalytic $CO_2$ conversion on various LDHs such as NiAl-LDH, ZnAl-LDH, NiGa-LDH, ZnLn-LDH, MgAl-LDH, *etc.*, greatly expanding the photocatalytic application of LDH materials.

In recent years, LDHs have shown great potential in the design and manufacture of nanomaterials for photocatalytic reduction of $CO_2$ due to their versatility in composition, morphology and structure, as well as their unique structural properties. However, over the past five years, there have been relatively few studies on the use of LDH materials in photocatalytic reduction to produce $CH_3OH$. It has been found that the photocatalytic activity of single LDH materials is limited by the rapid recombination of photogenerated carriers and their weak $CO_2$ adsorption and activation abilities, making them difficult to apply directly to photocatalytic $CO_2$ reduction. Therefore, further modifications are often necessary for these materials to achieve higher photocatalytic efficiency. Ziarati *et al.*[13] designed a 3D yolk@shell structure $TiO_2$/LDH containing oxygen vacancies through morphology control (Fig. 3). This structure is special in that it has a specific void space between the core and the shell, providing high light reflection potential and reduced diffusion resistance, as well as performance adjustability, which offers various opportunities for photocatalysis. In addition, the interior pore space can be used as a nanoreactor and enable efficient

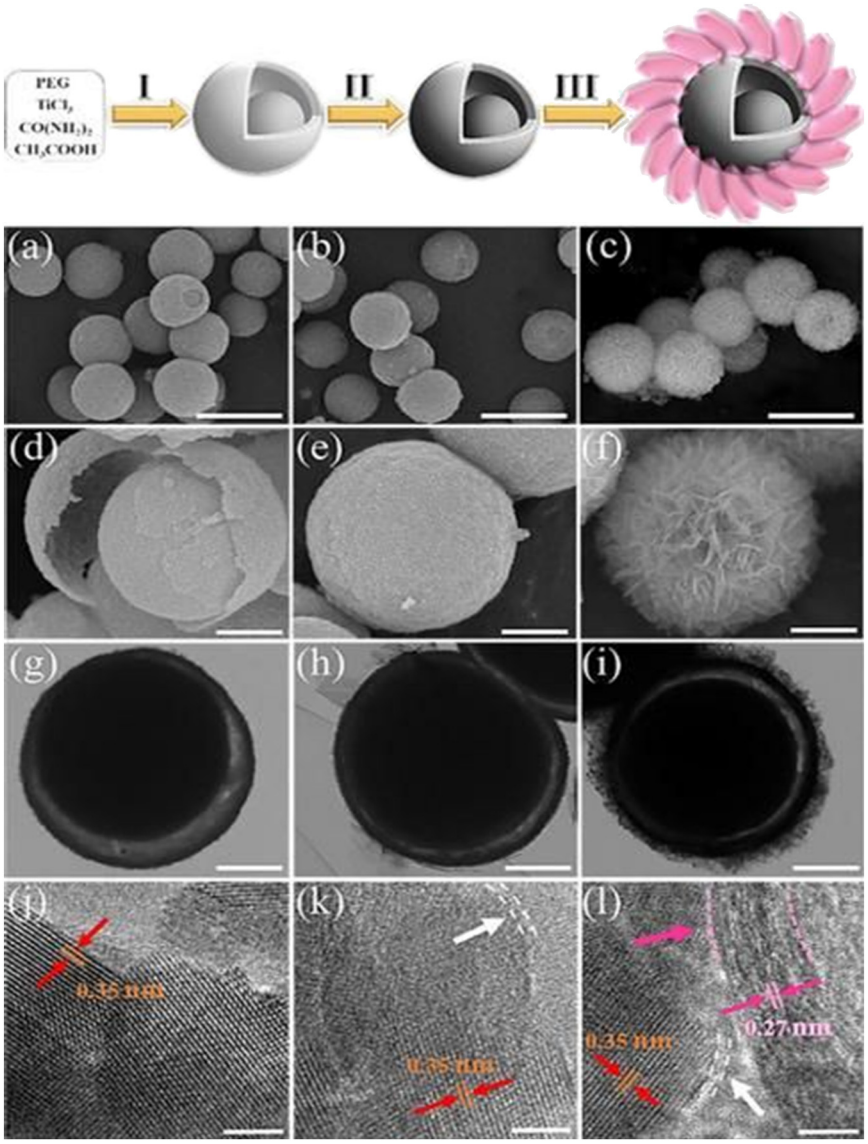


Fig. 3 Overall flowchart for the fabrication of the 3D Y@S $TiO_{2-x}$/LDH architecture (steps I–III); corresponding (a–f) FESEM, (g–i) TEM, and (j–l) HRTEM images of the 3D Y@S $TiO_{2-x}$/LDH sites.[13]

diffusion of solvents, substrates, and products through the porous surface. This structure reveals the high efficiency of photoreduction of $CO_2$ into a solar fuel in the absence of a precious metal co-catalyst. Its experiments showed that the generation of $CH_3OH$ was almost selective before 2 h, up to 251 μmol $g_{cat}^{-1}$ $h^{-1}$. To improve the efficiency of photocatalysis, many methods have been tried, such as atom doping,[14] defect engineering,[15] component control,[16] surface modification,[17] and heterojunction construction.[18] And the precise regulation of the intrinsic internal electric field of the photocatalyst through the construction of a heterojunction structure seems to be the most direct method for coordinating the separation of photogenerated carriers. Jiang *et al.*[19] prepared CuO quantum dot/ultra-thin CoAl-LDH (CuO/CoAl-u) direct Z-type 0D/2D heterojunctions by a simple electrostatic self-assembly process for photocatalytic $CO_2$ reduction. The results showed that the 4.5% CuO/CoAl-u heterojunction exhibited excellent photocatalytic performance, with a $CH_3OH$ yield of 283.26 μmol $g^{-1}$ $h^{-1}$, which is higher than the original CoAl-u. This enhanced photocatalytic performance is due to the outstanding light absorption properties of CuO/CoAl-u, the efficient separation of photoinduced carriers, and the high reduction capacity.

Overall, although a single LDH material may have limitations in the efficiency of photocatalytic $CO_2$ reduction, its unique layered structure and the versatility of interlayer anions and cations offer significant potential for developing new photocatalysts. The efficiency of converting $CO_2$ to $CH_3$-OH can already be greatly enhanced through various modification methods. However, these structural modifications increase the material's complexity, making it more challenging to understand the photocatalytic

 

mechanism. Employing advanced technologies to achieve precise micro-level regulation of the material structure could help address this issue.

### 3.2 Graphitic carbon nitride (g-$C_3N$)-based photocatalyst

g-$C_3N_4$ is a covalent solid mainly composed of carbon and nitrogen, forming a planar two-dimensional sheet structure similar to graphene. It is composed of two basic units, the triazine ring ($C_3N_3$) and the 3-*s*-triazine ring ($C_6N_7$), with the two-dimensional nanosheets bound by van der Waals forces. As a metal-free polymer N-type semiconductor, g-$C_3N_4$ possesses unique electrical, optical, structural and physicochemical properties. Unlike many other semiconductors, g-$C_3N_4$ offers a wide range of prospects for the development of novel nanostructured g-$C_3N_4$ photocatalysts due to its unique polymerization structure, shape, size, composition, thickness, and pore size and distribution.[20,21] Back in 2009, Wang *et al.*[22] discovered that g-$C_3N_4$ can produce hydrogen from water under visible light irradiation in the presence of a donor. This discovery opened a new chapter for g-$C_3N_4$-based photocatalysts and since then, they have garnered increasing global attention. The photocatalytic performance of g-$C_3N_4$ has been greatly enhanced through various modifications. In recent years, many important breakthroughs have been made in the synthesis and application of g-$C_3N_4$-based photocatalysts.

It has been reported that the selectivity to certain products can be influenced by changing the energy of CB electrons. Zero-dimensional (0D) semiconductor quantum dots have attracted significant attention due to their unique advantages such as large surface area, high atomic utilization, and short effective charge transfer length. One of the most important characteristics of 0D semiconductor quantum dots is their tunable band structures, which can be used to control the evolution of specific products through quantum confinement effects. Inspired by this, Li *et al.*[23] designed and prepared a g-$C_3N_4$/CdSe quantum dot (p-CNCS) photocatalyst with different CdSe particle sizes for highly selective and highly active photocatalytic $CO_2$ reduction. The synthesized CdSe quantum dots had a statistical diameter ranging from 1.2 to 4.1 nm. Based on the quantum confinement effect, the energy of CB electrons was adjusted to an appropriate value, inhibiting the formation of $H_2$ and promoting the formation of $CH_3OH$, thereby enhancing product selectivity. The final results showed that when the size of CdSe quantum dots was 2.2 nm, the selectivity to $CH_3OH$ reached 73% with a formation rate of 186.4 μmol $g^{-1}$ $h^{-1}$.

Although g-$C_3N_4$ exhibits excellent photocatalytic activity, its pure form suffers from rapid recombination of photogenerated electron–hole pairs, which significantly hampers its photocatalytic efficiency. To address these issues, the combination of g-$C_3N_4$ with heterojunction semiconductors can promote electron–hole separation, effectively preventing charge recombination. Liang *et al.*[24] designed a hollow structure g-$C_3N_4$@$CeO_2$ photocatalyst with oxygen-rich vacancies by combining the advantages of the heterostructure, oxygen-rich vacancies and hollow structure. Its unique hollow structure enabled light to be reflected and utilized multiple times within its inner cavity, ultimately improving the utilization efficiency of light. As the result, this novel photocatalyst demonstrated high $CO_2$ reduction capacity, with a $CH_3OH$ yield of 5.2 μmol $g^{-1}$ when the $CeO_2$ mass fraction was 49.7 wt%. Similarly, in order to improve the photocatalytic performance of g-$C_3N_4$, Li *et al.*[25] considered the strong adsorption capacity of MgO, an alkali metal oxide, for $CO_2$, as well as the use of precious metals (such as Au, Ag, Pt and Pd) as electron traps to improve the separation efficiency of photogenerated electron–hole pairs. They prepared a series of MgO-modified g-$C_3N_4$ composites by calcination and then loaded the Au cocatalyst onto the composite using the $NaBH_4$ reduction method. Under simulated solar illumination, the $CO_2$ reduction was studied by using the ternary photocatalyst. The results showed that the enhanced photocatalytic activity of the photocatalyst is due to the synergistic action between the components. Among them, the g-$C_3N_4$ photocatalyst co-modified with 3% MgO had the best photocatalytic performance, and $CH_3OH$ could reach 47.2 μmol $g^{-1}$ when the reaction time was 3 h.

The photocatalytic reduction of $CO_2$ to $CH_3OH$ is a process involving multi-electron transfer. During the electron transfer process, it is easy to produce other products requiring fewer electrons and protons, such as CO, HCHO, HCOOH, *etc.* To achieve the selective production of $CH_3OH$ by photocatalytic $CO_2$ reduction with high activity, Ma *et al.*[26] prepared a CN supported cobalt sulfide (CS) reduced photocatalyst, which can target the activation of $H_2O$ and induce the selective production of $CH_3OH$. The results showed that the selectivity to $CH_3OH$ (87.2%) was 2.3 times higher than that of CN (38.6%), and the $CH_3OH$ yield increased from 22.0 to 97.3 μmol $g^{-1}$ $h^{-1}$. As potential photocatalysts for $CO_2$ reduction, metal semiconductor oxide photocatalysts have been receiving significant attention. However, these photocatalysts often suffer from metal leaching caused by photocorrosion, which can lead to environmental pollution. To address this issue, Ding *et al.*[27] developed a metal-free core–shell photocatalyst composed of graphite carbon nitride (g-$C_3N_4$, CN) covalently attached to a melamine–resorcinol–formaldehyde (MRF) microsphere polymer. Under reaction conditions of 80 °C and 0.5 MPa, the $CH_3OH$ yield was 0.99 μmol $h^{-1}$. This yield was approximately 20 and 10 times that of its components CN and MRF, respectively. The external quantum efficiency ranged from 5.5 to 1.7% at wavelengths of 380 to 550 nm.

The development of g-$C_3N_4$ in photocatalytic $CO_2$ reduction is severely limited by the fast quenching rate of its photogenic carrier and its poor adsorption capacity of $CO_2$. The number of photogenerated electrons received by $CO_2$ is highly dependent on the close contact between the two. Therefore, one of the ideal ways to improve the $CO_2$ conversion rate is to increase the adsorption capacity of g-$C_3N_4$ for $CO_2$. Wang *et al.*[28] synthesized a new type of g-$C_3N_4$/

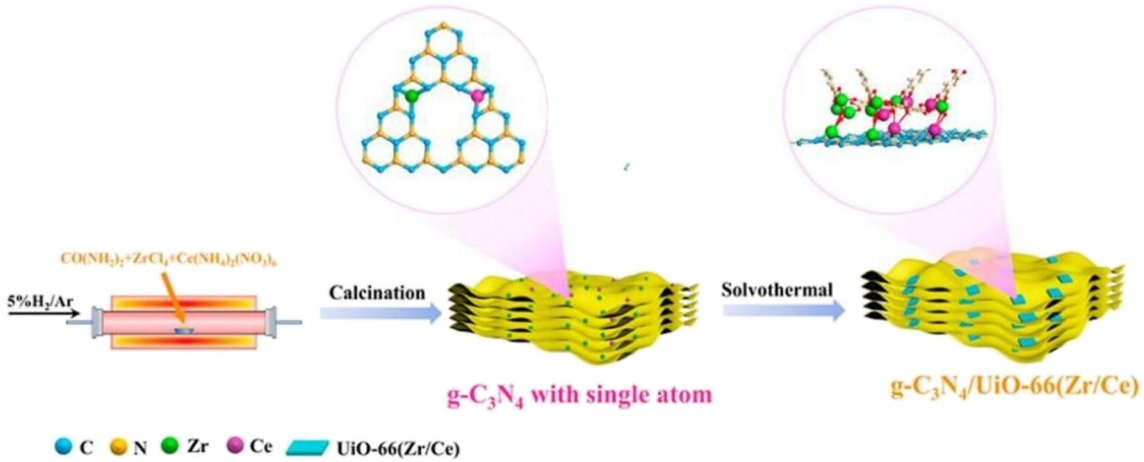


Fig. 4 Synthesis process of the g-$C_3N_4$/UiO-66 (Zr/Ce) photocatalyst.[28]

UiO-66 (Zr/Ce) nanosheet using an *in situ* method. As shown in Fig. 4, the g-$C_3N_4$ and UiO-66 interfaces are connected by N–Zr/Ce–O bonds. This two-dimensional structure tightly connected by chemical bonds accelerates the transport of electrons and significantly inhibit the quenching of photogenerated carriers. In Fig. 5b, UiO-66 (Zr/Ce) nanosheets form close contact with g-$C_3N_4$. The TEM results (Fig. 5d) also show that UiO-66 (Zr/Ce) and g-$C_3N_4$ have been successfully combined, with the edges of the UiO66 (Zr/Ce) nanosheets being almost transparent, indicating an ultra-thin thickness. The results of high-angle toroidal dark-field scanning transmission electron microscopy (HAADF-STEM) and the distribution of EDS components indicate that C, N, O, Zr and Ce are evenly distributed (Fig. 5e–j). It can be clearly found that Zr, Ce and O are mainly concentrated in the same region, and no obvious signals of Zr, Ce and O are found elsewhere. This shows that Zr, Ce, and O originate from UiO-66 (Zr/Ce), rather than the single atoms of Zr and Ce scattered on g-$C_3N_4$. In summary, individual atoms (Zr and Ce) successfully come together in UiO-66 (Zr/Ce) to form metal nodes through the connection of organic ligands. After that, $CO_2$ photocatalytic reduction experiments were carried out in an acetonitrile–water mixed system without adding a sacrificial agent. As shown in Fig. 6, the product yield of $CO_2$ photocatalytic reduction by g-$C_3N_4$/UiO-66 (Zr/Ce) was much higher than that by g-$C_3N_4$ and UiO-66 (Zr/Ce), and compared with photocatalysts of other systems, g-$C_3N_4$/UiO-66 (Zr/Ce) showed excellent performance in photocatalytic reduction of $CO_2$ to produce $CH_3OH$ and $C_2H_5OH$. In particular, after many cycles of experiments, the photocatalyst still showed good photocatalytic performance, indicating that it has excellent chemical stability.

In general, the photocatalytic performance of the modified g-$C_3N_4$ is greatly improved. Currently, commonly used modification methods can be categorized into surface modification, morphology control, doping, and hybrid formation, among others. In addition to the development of conventional binary systems, g-$C_3N_4$-based photocatalysts with ternary or multicomponent systems have also emerged in recent years. Table 1 shows the reduction of $CO_2$ to $CH_3OH$ by different g-$C_3N_4$-based photocatalysts in recent years. It can be seen from the table that whether in a binary system or ternary system, people are more inclined to choose metal compounds to modify g-$C_3N_4$. This is because the surface of metal compounds often has abundant active sites, so their catalytic performance is very prominent. In addition, after

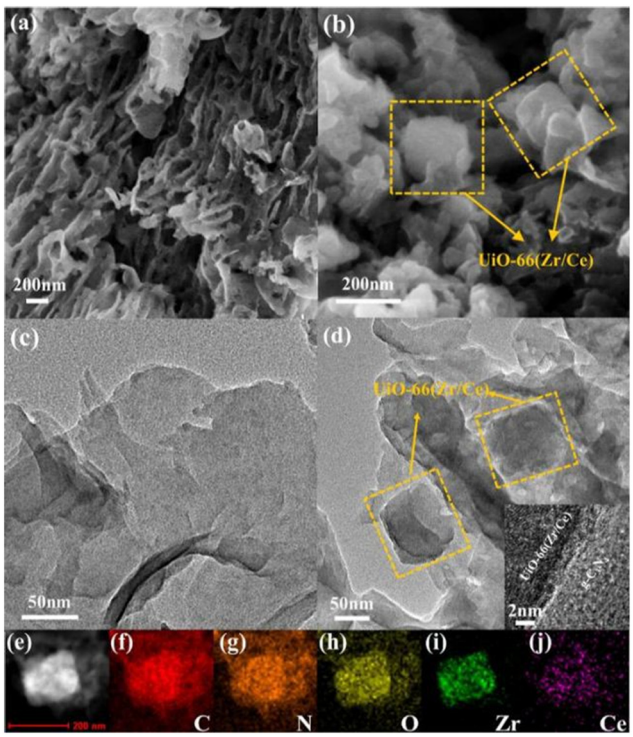


Fig. 5 SEM images of (a) g-$C_3N_4$ and (b) g-$C_3N_4$/UiO-66 (Zr/Ce); TEM images of (c) g-$C_3N_4$ and (d) g-$C_3N_4$/UiO-66 (Zr/Ce); (e–j) EDS mapping of g-$C_3N_4$/UiO-66 (Zr/Ce).[28]

 

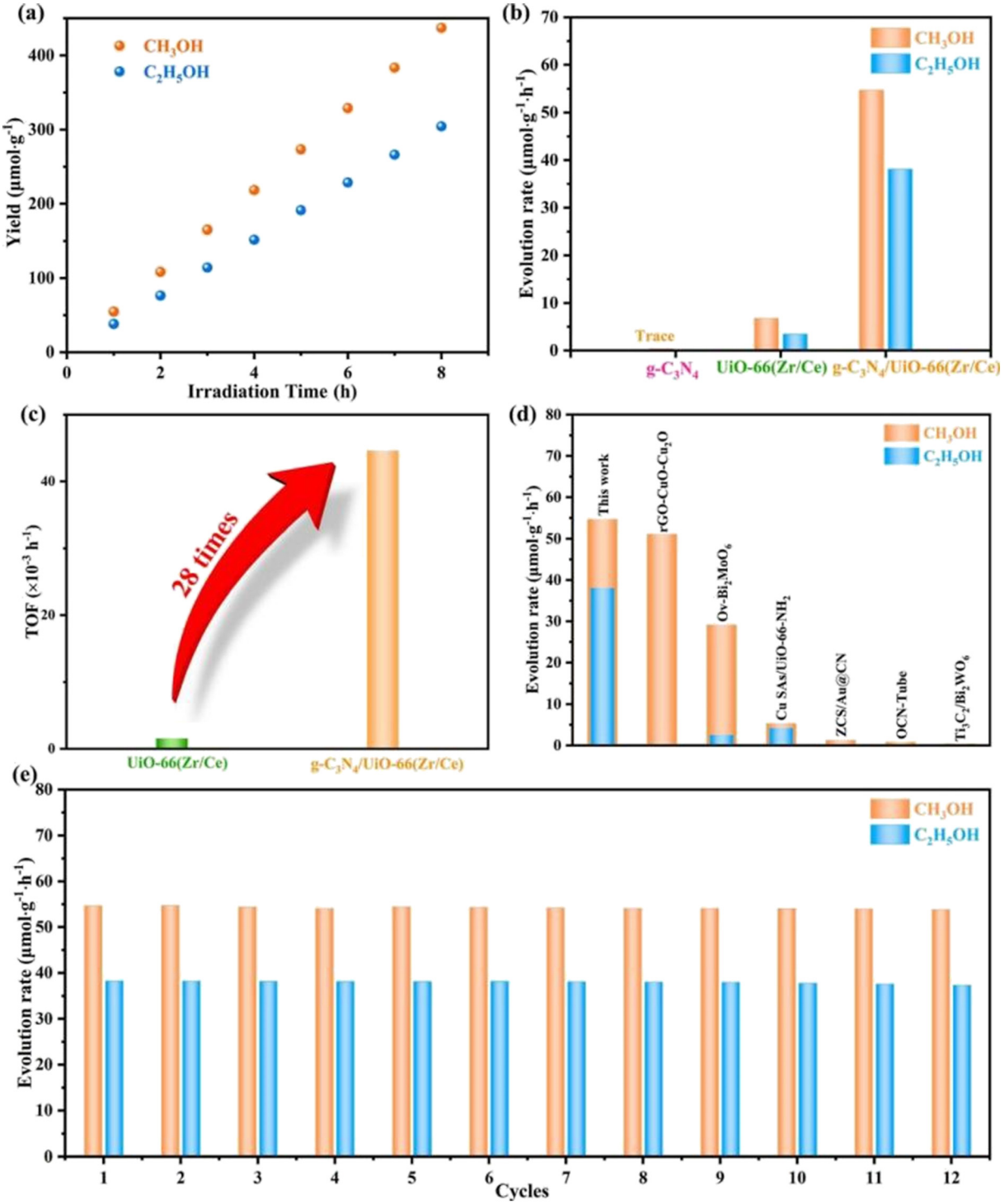


**Fig. 6** (a) Production of $CH_3OH$ and $C_2H_5OH$ on g-$C_3N_4$/UiO-66 (Zr/Ce). (b) Evolution rate of $CH_3OH$ and $C_2H_5OH$ on UiO-66 (Zr/Ce), g-$C_3N_4$, and g-$C_3N_4$/UiO-66 (Zr/Ce). (c) TOF of UiO-66 (Zr/Ce) and g-$C_3N_4$/UiO-66 (Zr/Ce). (d) Comparison of the yields of $CH_3OH$ and $C_2H_5OH$ with other photocatalysts. (e) Catalytic cyclic tests of g-$C_3N_4$/UiO-66 (Zr/Ce).[28]

the semiconductor is excited by light, because the work function of the metal is higher than that of the semiconductor material, the electrons migrate to the loaded metal and are trapped, which can inhibit the recombination of electron–hole pairs, thereby improving the efficiency of the photocatalytic reaction.

### 3.3 Graphene oxide (GO)-based photocatalyst

GO is a very important derivative of graphene-based materials, which is generally prepared by stripping graphite with acid. As a two-dimensional layered material, its structure extends to tens of microns in transverse dimensions.

**Table 1** Reduction of $CO_2$ to $CH_3OH$ by different g-$C_3N_4$-based photocatalysts

| Photocatalysts | Reaction conditions | $CH_3OH$ yield | Ref. |
|---|---|---|---|
| g-$C_3N_4$/CdSe | Visible light ($\lambda > 420$ nm) | 186.4 μmol $g^{-1}$ $h^{-1}$ | 23 |
| g-$C_3N_4$@$CeO_2$ | Monochromatic light (525 nm)/4 h | 5.2 μmol $g^{-1}$ | 24 |
| MgO/Au@g-$C_3N_4$ | Xenon lamp (300 W)/3 h | 47.2 μmol $g^{-1}$ | 25 |
| CoS/g-$C_3N_4$ | Xenon lamp (300 W) | 97.3 μmol $g^{-1}$ $h^{-1}$ | 26 |
| g-$C_3N_4$–melamine–resorcinol Formaldehyde | Xenon lamp with a 420 nm cut-off filter/5 h | 0.99 μmol $h^{-1}$ | 27 |
| g-$C_3N_4$/UiO-66 (Zr/Ce) | Xenon lamp (300 W) | 54.71 μmol $g^{-1}$ | 28 |
| ZnV O/RGO/g-C N | Xenon lamp (35 W) | 3488 μmol $g^{-1}$ | 29 |
| g-$C_3N_4$/$Sn_2S_3$-DETA | Visible light ($\lambda > 420$ nm) | 1.35 μmol $g^{-1}$ $h^{-1}$ | 30 |
| $Zn_{0.2}Cd_{0.8}S$/g-$C_3N_4$ | Xenon lamp (300 W) | 11.5 ± 0.3 μmol $g^{-1}$ $h^{-1}$ | 31 |
| Br/g-$C_3N_4$ | Xenon lamp (300 W)/1 h | 0.6 μmol $g^{-1}$ | 32 |
| Cu/P/g-$C_3N_4$/$TiO_2$ | 20 W LED light | 859 μmol $g_{cat}^{-1}$ | 33 |
| Ag/UiO-66@g-$C_3N_4$ | UV light ($\lambda < 380$ nm)/2 h | 17.76 μmol $g^{-1}$ $h^{-1}$ | 34 |

Although it lacks the highly conjugated structure of graphene, the oxidation process makes the base surface and edge of GO modified by a variety of oxygen-containing functional groups.[35] This modification provides numerous active sites and a larger specific surface area for the surface of graphene oxide materials. Additionally, GO materials can modulate their electrical conductivity and band gap by regulating the type and number of oxygen-containing functional groups they contain, which greatly expands their range of applications. In photocatalytic systems, GO can be used as both a cocatalyst and a photocatalyst. As a semiconductor, it has a low degree of oxidation and an inherently wide bandgap. Furthermore, its bandgap width can be adjusted by changing its C/O ratio and the type and number of oxygen-containing functional groups it contains.[36]

Unlike graphite, GO is hydrophilic due to its surface oxygen-containing groups, which enhances its dispersion in water. Given that GO is a polymer-like graphite semiconductor composed solely of carbon, oxygen, and hydrogen, with a large surface area, Yeh *et al.*[37] suggested that these structural characteristics should enhance GO's effectiveness as a photocatalyst for $H_2$ generation from water. In 2010, they synthesized a GO semiconductor photocatalyst using an improved Hummers method, achieving an apparent band gap ranging from 2.4 to 4.3 eV. They found that under ultraviolet or visible light irradiation, the GO photocatalyst could stably catalyze $H_2$ production from a 20 vol% methanol solution and pure water. This study demonstrated for the first time the potential of graphene-based materials as a medium for water decomposition by sunlight. GO-based photocatalytic composites have significant advantages in the field of photocatalysis due to their unique layered structure. In recent years, the research on GO-based photocatalysts in the field of photocatalytic $CO_2$ reduction has mainly used metal oxides and GO to form composite materials, or used GO as a cocatalyst to improve the photocatalytic performance of photocatalytic materials. For example, Shi *et al.*[38] synthesized a series of $In_2O_3$–GO composite photocatalysts modified by GO by a precipitation method. The effect of different contents of graphene oxide on the activity of $CO_2$ hydrogenation to $CH_3OH$ by the $In_2O_3$–GO photocatalyst was studied. The results showed that GO can promote the transformation of cubic $In_2O_3$ (c-$In_2O_3$) to hexagonal $In_2O_3$ (h-$In_2O_3$) during $CO_2$ hydrogenation and form a homojunction between h-$In_2O_3$(110) and c-$In_2O_3$(440), which strengthens the interaction between the two phases. Thus, the reduction of $In_2O_3$ and the formation of oxygen vacancies on the surface are promoted, which is greatly conducive to the formation of methanol. When the content of GO reaches 8%, the space time yield (STY) of methanol can be as high as 0.93 $g_{MEOH}$ $h^{-1}$ $g^{-1}$, and the selectivity can reach more than 76%. Zhang *et al.*[39] prepared 2D/2D nanostructures

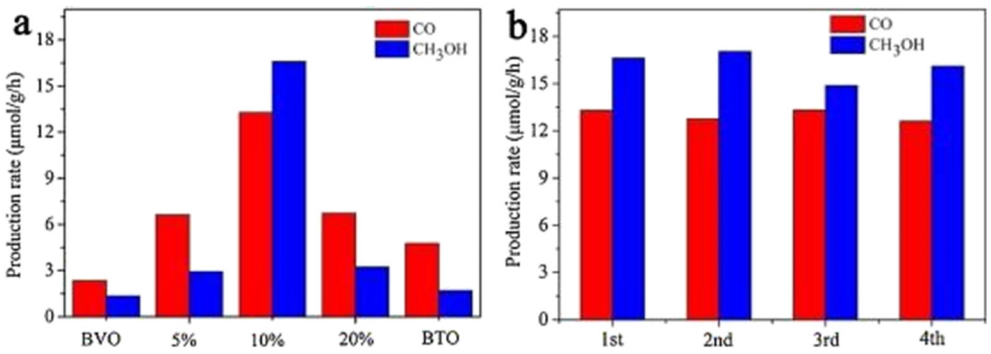


**Fig. 7** (a) $CH_3OH$ and CO evolutions on $BiVO_4$/$Bi_4Ti_3O_{12}$ with different $Bi_4Ti_3O_{12}$ contents under a 300 W Xe lamp and (b) photocatalytic activity stability of the $BiVO_4$/10% $Bi_4Ti_3O_{12}$ sample within 12 h with 3 h per circulation.[52]

 

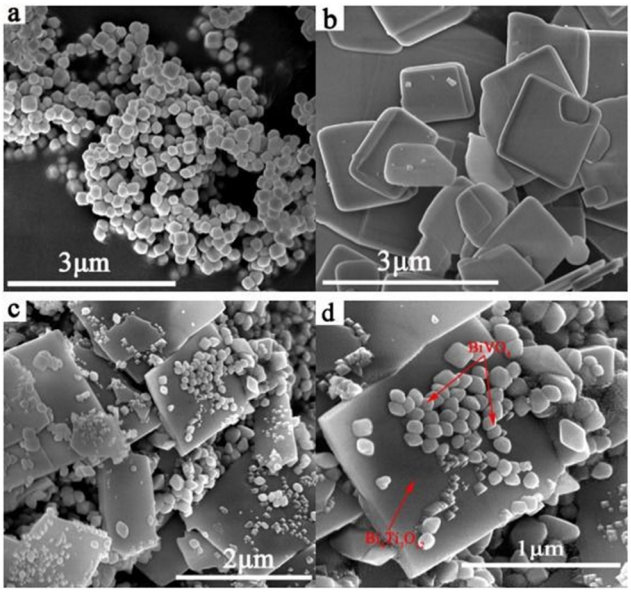


Fig. 8 SEM images of (a) $BiVO_4$, (b) $Bi_4Ti_3O_{12}$, and (c and d) $BiVO_4$/10% $Bi_4Ti_3O_{12}$.[52]

composed of $BiVO_4$ and layered GO by a hydrothermal method and realized the efficient effect of $CO_2$ photoreduction to $CH_3OH$. The optimized 10-CGO/$BiVO_4$ composite catalyzed $CO_2$ reduction to produce $CH_3OH$ under light, which was 537.78 μmol $g^{-1}$ $h^{-1}$, about 6.47 times that of $BiVO_4$ nanosheets. In addition, multi-component GO based photocatalysts[39–43] have also been constructed by doping and composite methods. Due to their unique 2D or 3D structure, they have shown excellent performance in selectively capturing $CO_2$ and driving $CO_2$ reduction.

In general, GO materials have significant advantages in the field of photocatalysis due to their huge specific surface area, zero band gap width, 2D-layered structure and other characteristics.[44,45] However, at present, there are few studies on low-cost, mass-produced GO materials, which has limited their application scope to some extent, so there is an urgent need to conduct in-depth research on this class of materials. However, to solve this problem, the integration of resources appears to be very critical, to build a more reasonable industrial ecological chain system and to avoid the waste of resources in order to be more conducive to in-depth research.

### 3.4 Mixed metal compound photocatalyst

Metal oxides are a common class of compounds in daily life. Because of their excellent stability and good electrical conductivity, they have been widely studied as effective photocatalysts. In the process of photocatalytic $CO_2$ reduction, the most important thing is the separation and transfer of electron–hole pairs. Therefore, the band gap width of the photocatalyst and the potential corresponding to the conduction band and valence band are the key factors determining the photocatalytic efficiency.[46] Due to the wide

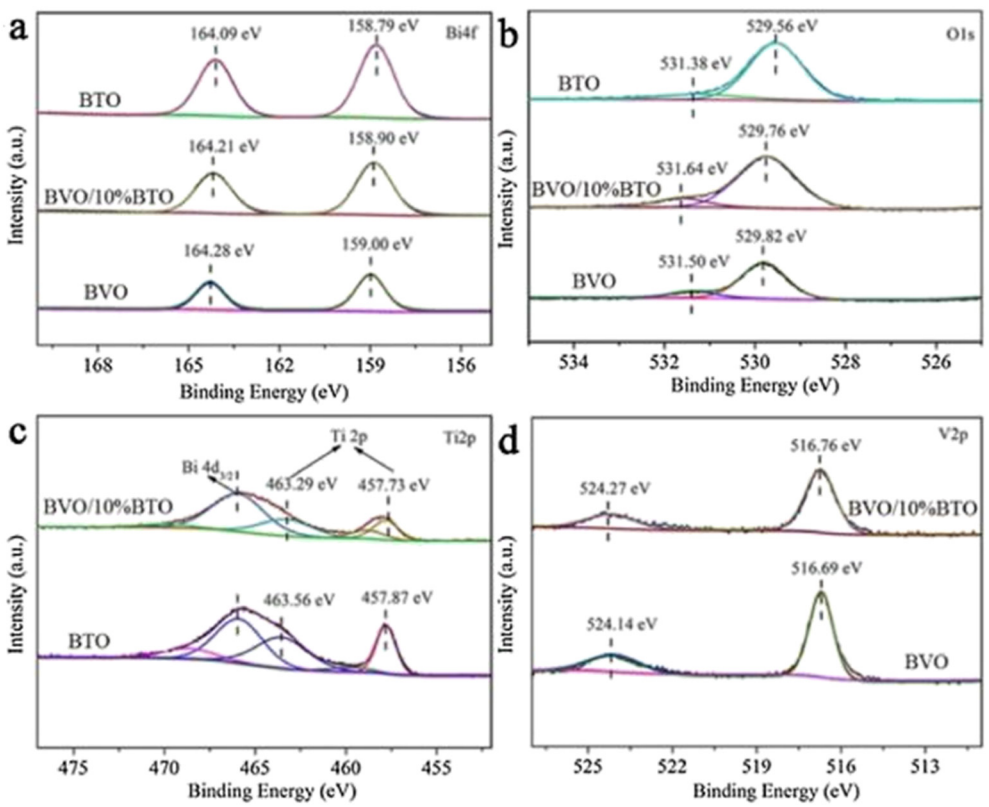


Fig. 9 The Bi 4f (a), O 1s (b), Ti 2p (c) and V 2p (d) spectra of $BiVO_4$, $BiVO_4$/10% $Bi_4Ti_3O_{12}$ and $Bi_4Ti_3O_{12}$.[52]

variety of metal oxides, their band gap width and redox potential are adjustable in a wide range, which makes them have broad application prospects in the field of photocatalysis. Metal oxides have two electronic configurations: $d^0$ (transition metal) and $d^{10}$ (main group metal). Among them, the transition metals that can form metal oxides mainly include $Ti^{4+}$, $Zn^{2+}$, $Zr^{4+}$, $Ta^{5+}$, $Nb^{5+}$, $W^{6+}$ and $Mo^{6+}$, and the main group metals mainly include $In^{3+}$, $Ga^{3+}$, $Ge^{4+}$, $Sn^{4+}$ and $Sb^{5+}$.[47]

$TiO_2$ is a widely used semiconductor material in various fields, including hydrogen production, carbon dioxide conversion, organic pollutant degradation, and water purification, where it plays a highly significant role. This is because $TiO_2$-based materials have good light absorption performance and stability under UV-visible light irradiation.[46] As early as 1972, Fujishima *et al.*[48] found for the first time that $TiO_2$ catalyzed the $H_2O$ redox reaction under light irradiation. This research has opened the prelude to the study of photocatalytic materials. However, $TiO_2$, due to its wide band gap (3.2 eV), has a very low utilization of visible light in the UV-visible region and can only absorb a small part of ultraviolet light. This limits the wide application of $TiO_2$ in the field of high efficiency photocatalysis. As research progresses, a variety of metal compound photocatalytic materials have been developed. Some of the most common include ZnO, CdS, $Fe_2O_3$, $WO_3$, ZnS, BiOBr, $Ag_3PO_4$, *etc.*[49] However, simple photocatalytic materials often have some shortcomings such as low photoresponse, high recombination rate of photogenerated electron pairs and low photocatalytic efficiency. In addition, photocatalytic systems in which metal compounds and organic compounds are constructed into composites have

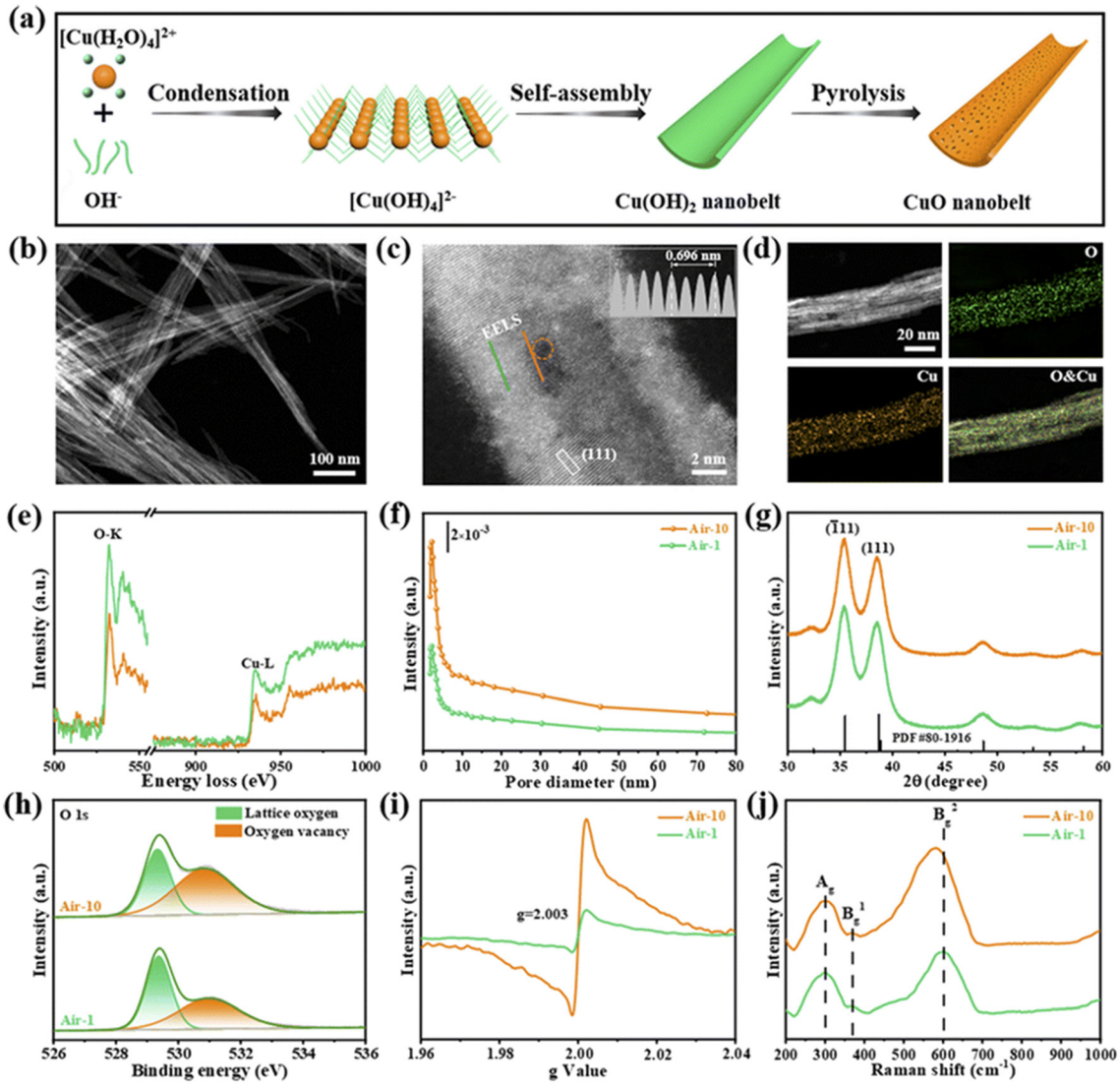


**Fig. 10** (a) Schematic illustration of the synthetic process of a CuO nanobelt. (b) TEM image, (c) HAADF-STEM image (inset: intensity profiles recorded from the grey rectangular area), and (d) EDX elemental mappings of air-10. (e) EELS spectra for the O-K and Cu-L edges (the solid orange and green lines are from the corresponding scan lines in (c)). (f) The pore-size distribution curves, (g) XRD patterns, (h) O 1s XPS spectra, (i) EPR spectra, and (j) Raman spectra of air-1 and air-10.[53]

 

appeared,[50,51] but those that can reduce $CO_2$ to $CH_3OH$ are rare. In order to improve the photocatalytic efficiency, at present, people often use a variety of metal compound materials to construct heterojunctions, so as to promote the separation of photogenerated electron–hole pairs, accelerate charge transfer, and finally achieve efficient photocatalytic reactions.

Because of the differences in the extranuclear electron structure, different metal compounds have their own unique band gap structure. In general, two or more materials whose bandgap positions can be combined in a "misaligned" manner can be combined to form a heterojunction structure, which facilitates the transport of electron–hole pairs. There are three types of common heterojunctions, namely type-II heterojunctions, Z heterojunctions and S heterojunctions. The modes of electron–hole transport between different types of heterojunctions are different. But ultimately, it is for the same purpose, that is, to improve the separation of photogenerated electron–hole pairs, so as to improve the photocatalytic efficiency. At present, coupling two or more semiconductors into heterojunctions is considered as a promising method to obtain highly photocatalytically active photocatalysts. Wang *et al.*[52] synthesized $BiVO_4/Bi_4Ti_3O_{12}$ heterojunction composite materials by an *in situ* hydrothermal method. This novel composite material has excellent photocatalytic ability and can reduce $CO_2$ and $H_2O$ to $CH_3OH$ and CO. Among them, the $CH_3OH$ and CO yields of the $BiVO_4$/10% $Bi_4Ti_3O_{12}$ sample were the highest (Fig. 7a), up to 16.6 and 13.29 μmol $g^{-1}$ $h^{-1}$, which were 12.39 and 5.68 times higher than pure $BiVO_4$, and 9.88 and 2.80 times higher than pure $Bi_4Ti_3O_{12}$, respectively. In addition, the cyclic experiment results in Fig. 7b show that the photocatalytic stability of $BiVO_4$/10% $Bi_4Ti_3O_{12}$ is good. In Fig. 8c and d, $BiVO_4$ has successfully and uniformly grown on the surface of $Bi_4Ti_3O_{12}$. There was no apparent reunion. Afterwards, XPS analysis was performed (Fig. 9), which verified the electron transfer mechanism of the $BiVO_4$/10% $Bi_4Ti_3O_{12}$ sample by comparing the binding energies, *i.e.*, the electrons migrated from $BiVO_4$ to $Bi_4Ti_3O_{12}$, and a heterojunction was formed between $BiVO_4$ and $Bi_4Ti_3O_{12}$. This provides effective evidence to prove its photocatalytic ability.

Interface engineering often has outstanding performance in improving the efficiency of photocatalysis. This is because abundant catalytically active sites can be generated on the surface of the material through interface modification, thereby enhancing the adsorption capacity of the material for $CO_2$, while shortening the charge transfer distance, thus ensuring efficient electron–hole pair transport. Wang *et al.*[53] developed porous CuO ultra-thin nanoribbons with well-controlled oxygen vacancies ($V_o$) by a three-step method using wet chemical methods combined with rapid calcination strategies (Fig. 10). The ultrathin band structure of CuO, along with micropores and slight lattice perturbations, was confirmed *via* TEM and HAADF-STEM, indicating the

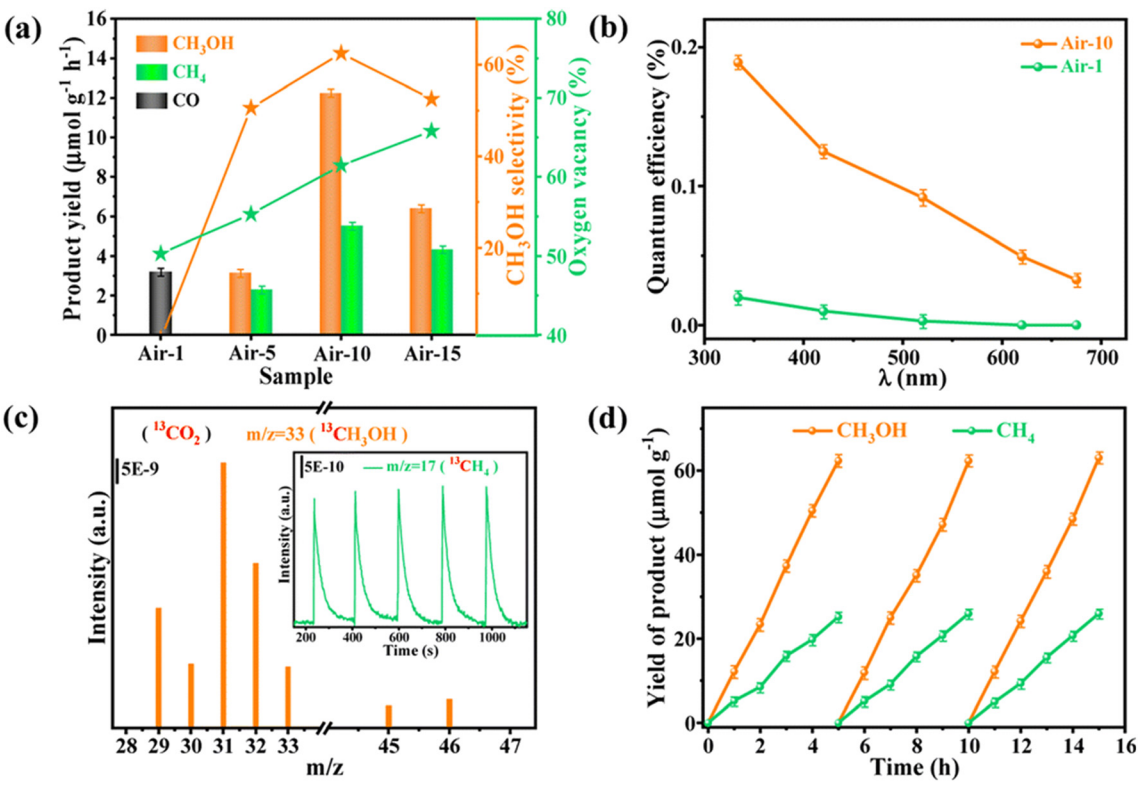


**Fig. 11** (a) Product yields, $CH_3OH$ selectivity and oxygen vacancy content of different photocatalysts. (b) QE values of air-1 and air-10, respectively. (c) GC-MS spectra of $^{13}CH_3OH$ and $^{13}CH_4$ generated from $^{13}CO_2$ photoreduction of air-10. (d) Photocatalytic stability of air-10.[53]

presence of point defects. Oxygen vacancies ($V_o$) were further investigated using various techniques, including low-loss EELS, XPS, and EPR. These defects enhanced the selective adsorption and enrichment of gas molecules on the photocatalyst surface during $CO_2$ reduction. The photocatalytic reaction achieved an optimal $CH_3OH$ generation rate of 12.3 μmol $g^{-1}$ $h^{-1}$ with a selectivity of 62.5%. Isotope labeling confirmed $CO_2$ as the carbon source, and cycling experiments demonstrated the material's good photostability (Fig. 11). Li *et al.*[54] developed V–$Bi_19Br_3S_{27}$, a nanowire photocatalyst with abundant Br and S double vacancies and surface Bi–O bonds, through alkali etching. Compared with the synthetic $Bi_{19}Br_3S_{27}$ nanowires, the treated nanowires V–$Bi_{19}Br_3S_{27}$ retained their original nanowire morphology (Fig. 12). EDS spectra analysis detected low-density oxygen in the structure. FT-XANES and EXAFS results revealed the formation of double vacancies, and EXAFS wavelet transform analysis confirmed the Bi–O bond formation in V–$Bi_{19}Br_3S_{27}$. Ultrafast transient absorption (TA) spectroscopy showed that both $Bi_{19}Br_3S_{27}$ and V–$Bi_{19}Br_3S_{27}$ nanowires have transient absorption peaks at 1150 nm, indicating NIR light excitation capability. The electron decay kinetics revealed that the V–$Bi_{19}Br_3S_{27}$ nanowires had a delay time 22 times longer than the

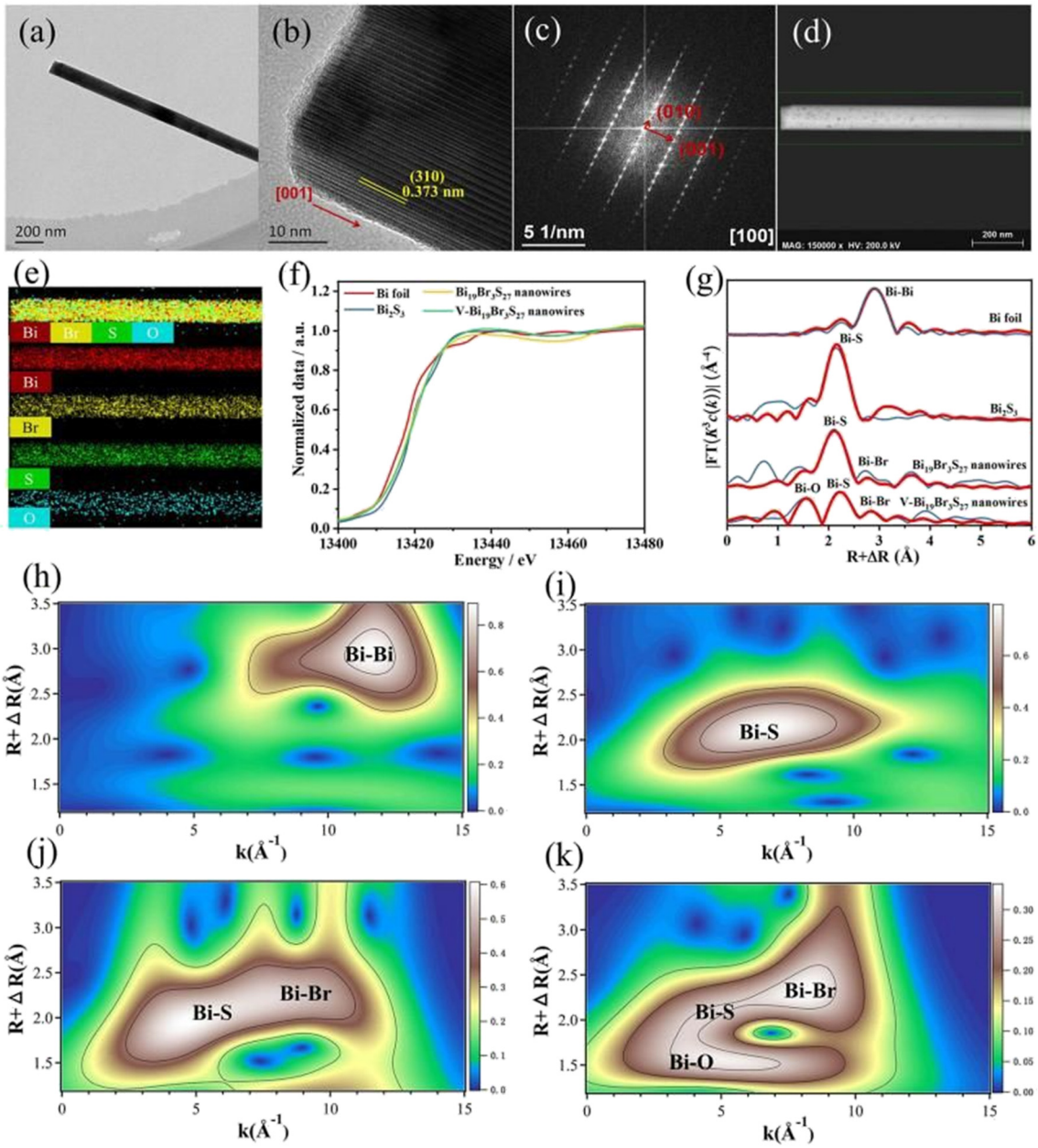


**Fig. 12** (a) TEM image, (b) HRTEM image, (c) SAED image, and (d and e) EDS mapping images of a V–$Bi_{19}Br_3S_{27}$ nanowire. (f) Bi $L_{III}$-edge XANES spectra of $Bi_{19}Br_3S_{27}$, V–$Bi_{19}Br_3S_{27}$ nanowires and bismuth references. (g) Corresponding Fourier transforms *R* space fitting results. Red: observed data; blue: fitted data. (h–k) Wavelet transforms for $k^2$-weighted EXAFS signals of Bi, $Bi_2S_3$, $Bi_{19}Br_3S_{27}$, and V–$Bi_{19}Br_3S_{27}$, respectively.[54]

$Bi_{19}Br_3S_{27}$ nanowires, suggesting that vacancy formation and oxygen doping enhanced the photogenerated electron lifetime. The resulting V–$Bi_{19}Br_3S_{27}$ nanowires produced 1.6 μmol $g^{-1}$ $CH_3OH$ in the photocatalytic reduction of $CO_2$ under near-infrared irradiation without any co-catalyst and sacrificial agent, which was 2.3 times higher than that of the $Bi_{19}Br_3S_{27}$ nanowires (Fig. 13).

At present, there are numerous research studies on mixed metal compounds in the field of photocatalysis. In this paper, we summarized the recent research results on the reduction of $CO_2$ to $CH_3OH$ by photocatalysts with different mixed metal compounds. As shown in Table 2, we find that most of these photocatalysts are composed of transition metal compounds, which can be divided into polymetallic oxides, polymetallic sulfides, and binary or multi-metal oxide composites. In the past few decades, a lot of research has been done on various photocatalytic materials, such as $TiO_2$, Cds, $Bi_2O_3$, $CeO_2$, *etc.* However, due to the single composition and structure of these photocatalysts, the overall photoconversion efficiency and product selectivity are often not ideal due to the rapid recombination of photogenerated holes in the process of photocatalytic $CO_2$ reduction. In order to improve the photocatalytic efficiency, it has been found that mixed metal compounds synthesized by hybridization,[55–58] etching,[54] surface reconstruction,[59,60] defect control,[53,61,62] and heterojunction construction[52,63] often have better photocatalytic properties than single metal compounds. This is similar to the study of alloys in order to improve the defects of pure metals in certain properties. However, it is not enough to focus only on the composition of the photocatalyst. In order to increase the specific surface area and obtain more $CO_2$ conversion active sites, it is necessary to pay attention to the homogeneity of the composite during the preparation process, as well as the dispersion of metal vacancies and oxygen vacancies on the surface of the material during the surface reconstruction and defect control process.

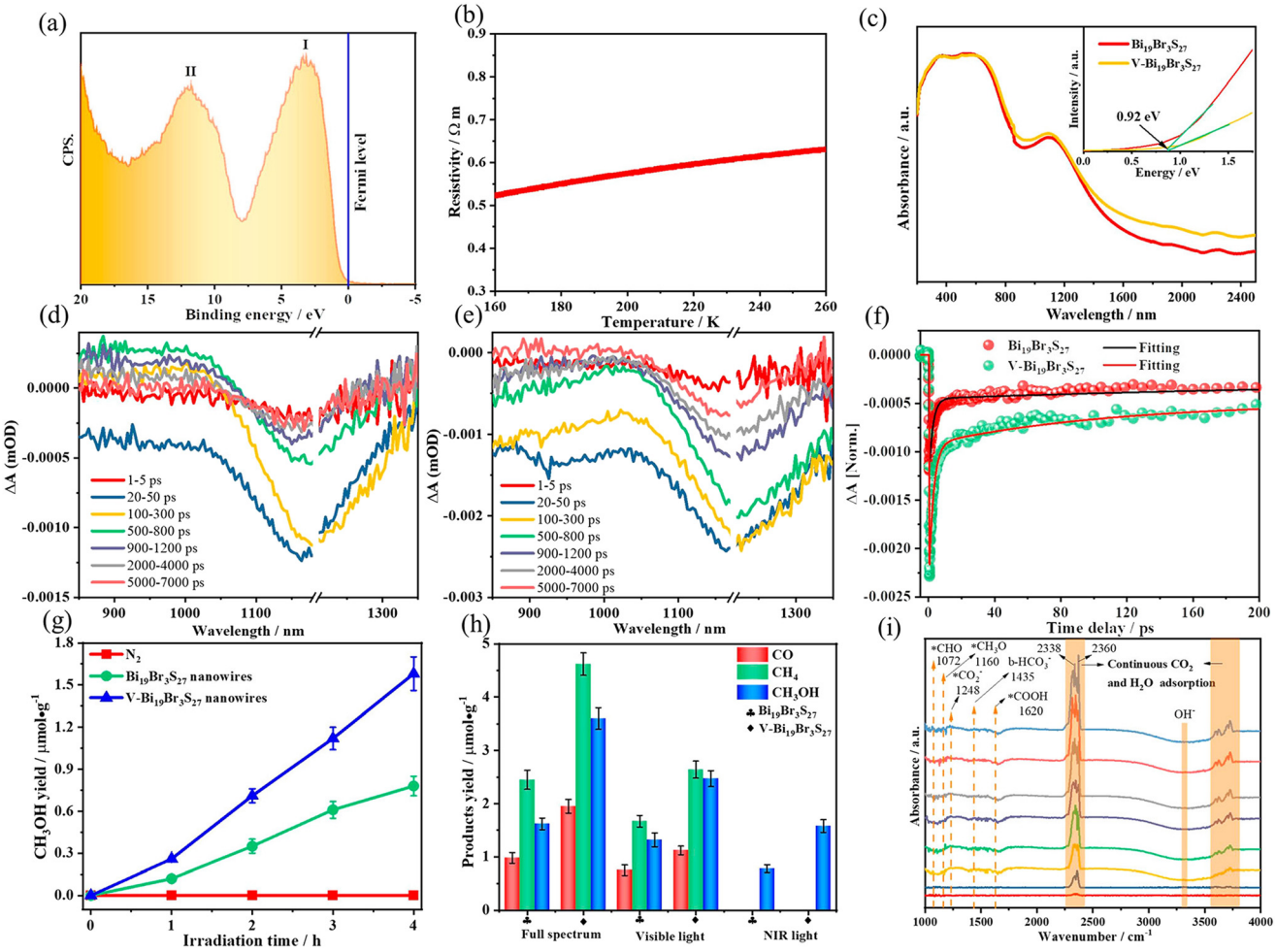


Fig. 13 (a) Valence band XPS spectrum and (b) temperature dependence of resistivities of V–$Bi_{19}Br_3S_{27}$ nanowires. (c) Optical absorption spectra and the corresponding optical bandgaps of $Bi_{19}Br_3S_{27}$ and V–$Bi_{19}Br_3S_{27}$ nanowires. Transient absorption (TA) spectra of (d) $Bi_{19}Br_3S_{27}$ and (e) V–$Bi_{19}Br_3S_{27}$ nanowires. (f) Corresponding TA kinetics. Photocatalytic $CH_3OH$ evolution under (g) NIR and (h) full-spectrum light irradiation for $Bi_{19}Br_3S_{27}$ and V–$Bi_{19}Br_3S_{27}$ nanowires. (i) *In situ* FT-IR spectra showing coadsorption of $CO_2$ and $H_2O$ on V–$Bi_{19}Br_3S_{27}$ nanowires.[54]

Table 2 Photocatalyst reduction of $CO_2$ to $CH_3OH$ with different mixed metal compounds

| Photocatalysts | Reaction conditions | $CH_3OH$ yield ($\mu mol\ g^{-1}\ h^{-1}$) | Ref. |
|---|---|---|---|
| $BiVO_4/Bi_4Ti_3O_{12}$ | Commercial xenon lamp (300 W) | 16.6 | 52 |
| CuO | Xenon lamp (300 W) | 12.3 | 53 |
| $Bi_{19}Br_3S_{27}$ | Xenon lamp (300 W) | 1.6 | 54 |
| $M_{0.33}WO_3$ | Xenon lamp (300 W) (Air as a carbon source) | 15.48 | 55 |
| $ZnO/Fe_2O_3$ | Xenon lamp (300 W) | 178.3 | 64, 65 |
| $Mo_2C/TiO_2$ | UV-visible LED lamp (5 mW $cm^{-2}$) | 11.8 | 63 |
| CuO | Visible LED lamp (25 °C) | 3.7 | 59 |
| $Mg(OH)_2/CuO/Cu_2O$ | Halogen lamp (20 W, 300–900 nm) | 6 | 66 |
| $CeO_2$ | Xenon lamp (300 W) | 0.702 | 61 |
| $VO_2/ZnV_2O_4$ | HID xenon lamp (35 W) | 202 | 67 |
| $CeO_2/ZnIn_2S_4$ | Xenon lamp (300 W) | 0.542 | 56 |
| $CoO/Co/TiO_2$ | Xenon lamp (300 W, 120 °C) | 39.6 | 68 |
| $MoS_2/Mn_{0.2}Cd_{0.8}S$ | Xenon lamp (300 W, 24 h) | 1017.7 | 57 |
| $NiSe_2/WSe_2$ | Xenon lamp (300 W) | 3.80 | 69 |
| $Cu_2O/TiO_2$ | UV light (6 h) | 21.0–70.6 | 70 |
| $NiMoO_4$ | LED light (20 W) | 3365 | 71 |
| Ce-MOF/$Bi_2MoO_6$ | Xenon lamp (300 W, 6 h) | 40.59 | 72 |
| $Bi_{12}SiO_{20}/BiO_{2-x}$ | Xenon lamp (300 W) | 31.16 | 73 |
| $LiNbO_3$ | UV pen lamp | 35 | 58 |
| $Bi_2O_2SiO_3$ | Xenon lamp (300 W, 4 h) | 12.78 | 60 |
| $CuCo_2O_4/CeO_2$ | Xenon lamp (300 W, 9 h) | 1320 | 74 |
| $WO_{3-x}$ | Monochromatic visible light (675 nm) | 17 | 62 |

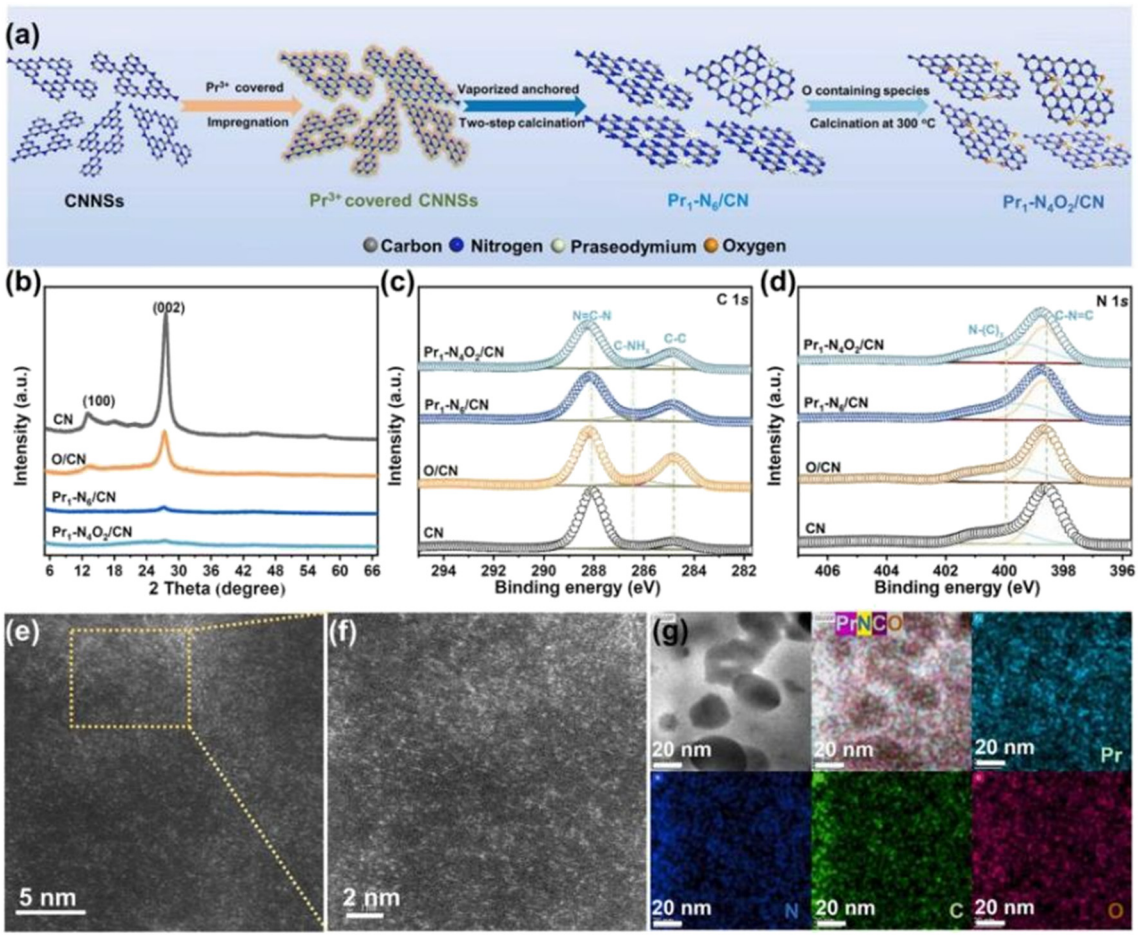


Fig. 14 Synthesis process and structural information of the as-fabricated photocatalysts. (a) Schematic of the synthesis process of $Pr_1$–$N_6$/CN and $Pr_1$–$N_4O_2$/CN; (b) XRD patterns; high-resolution XPS spectra of (c) C 1s and (d) N 1s over CN, O/CN, $Pr_1$–$N_6$/CN, and $Pr_1$–$N_4O_2$/CN; (e) and (f) AC-HAADF-STEM images, and (g) corresponding EDX mapping images of the as-prepared $Pr_1$–$N_4O_2$/CN.[77]

 

### 3.5 Single metal-doped photocatalyst

Single metal-doped photocatalysts mainly refer to the single metal as an impurity atom to modify the structure of metal compounds to form composite materials with efficient photocatalytic performance. Among them, the single metal is divided into two categories, one refers to precious metals, often as doping elements of precious metals which are: gold (Au), silver (Ag), platinum (Pt), palladium (Pd) and so on; the other category refers to non-precious metals, mainly including iron (Fe), cobalt (Co), nickel (Ni), copper (Cu) and so on. It has been reported that the successful doping of single Pd, Pt, Cd and Hg atoms into gold nanoparticles can not only enhance the stability of nanoparticles, but also adjust the catalytic performance of nanoparticles.[75] As for the application of single atom doping in the field of photocatalysis, as early as 2014, Xing *et al.*[76] stably synthesized dispersed metal atoms (Pt, Pd, Rh or Ru) on $TiO_2$ for the first time in order to solve the problem of the aggregation of precious metals as co-catalysts in the supported process or photocatalytic reaction. The dispersed metal atom-based photocatalyst has excellent hydrogen evolution stability, and its photocatalytic activity is 6–13 times higher than that of metal clusters supported on $TiO_2$ by traditional methods.

At present, various types of single metal doped photocatalytic materials are explored for photocatalytic $CO_2$ reduction. Ma *et al.*[77] synthesized $Pr_1$–$N_6$/CN photocatalysts using a "two-step calcination-induced metal vaporization strategy" (Fig. 14a). Then, using the same strategy, carbon nitride (CN)-loaded Pr monoatomic oxygen coordination materials were designed by adding oxygen-containing species. The engineered oxygen coordination configuration of the Pr monoatom ($Pr_1$–$N_4O_2$/CN) was successfully obtained and its ultra-high loading of Pr atoms is highly dispersed on the surface of the CN substrate. This photocatalyst utilizes oxygen atoms to modulate the electronic structure of a single Pr atom, which can be

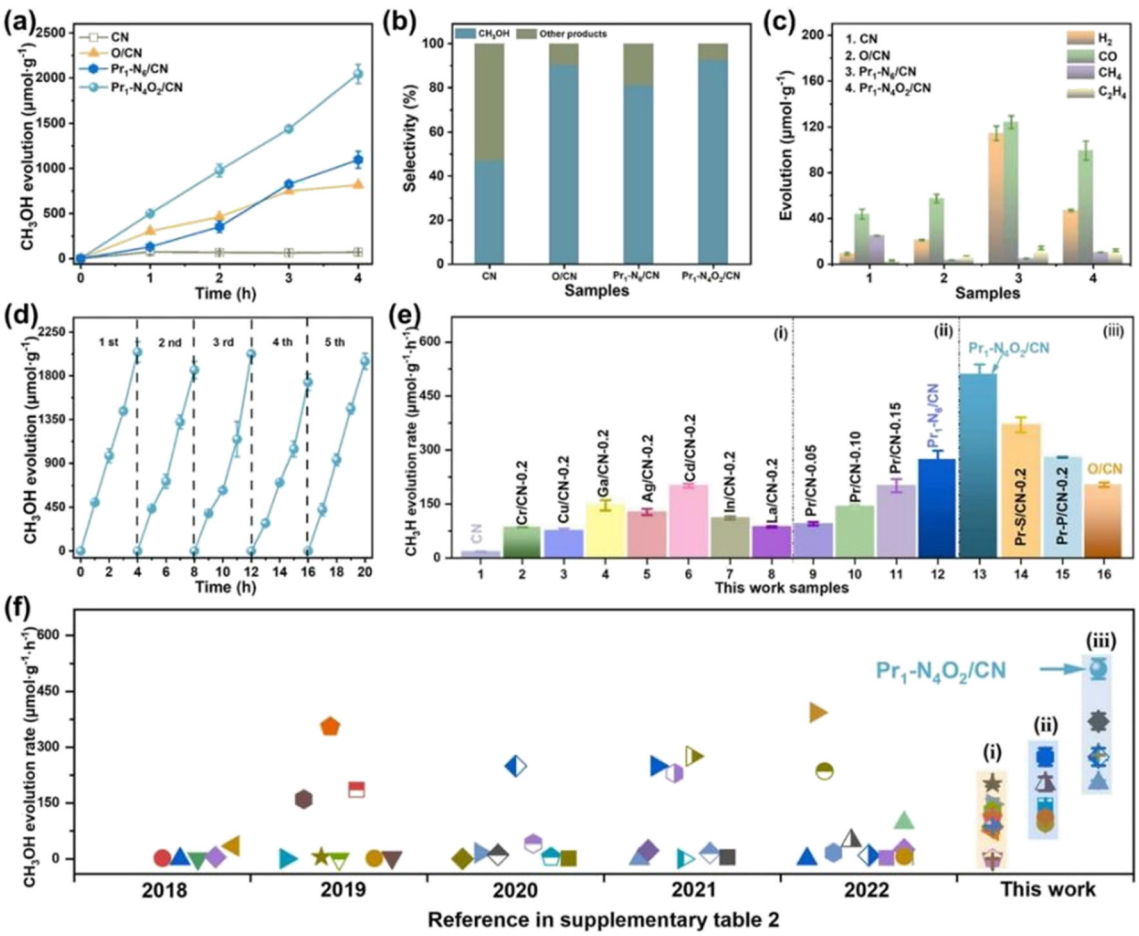


**Fig. 15** Photocatalytic reduction $CO_2$ performance of the as-prepared photocatalysts. (a) $CH_3OH$ production with time for CN, O/CN, $Pr_1$–$N_6$/CN, and $Pr_1$–$N_4O_2$/CN; (b) the selectivity to $CH_3OH$ and other products; (c) $H_2$, CO, $CH_4$, and $C_2H_4$ production in 4 h; (d) $CH_3OH$ production corresponding to cycle experiments (~20 h) for $Pr_1$–$N_4O_2$/CN; (e) $CH_3OH$ production of the reference photocatalysts synthesized in this work, such as (i) CN supported different kinds of metal elements, (ii) CN supported Pr single-atom with different density, and (iii) CN supported Pr single-atom with different coordination configurations; and (f) $CH_3OH$ evolution rate of various photocatalysts during photocatalytic reduction of $CO_2$ with $H_2O$ under similar reaction conditions over the past five years.[77]

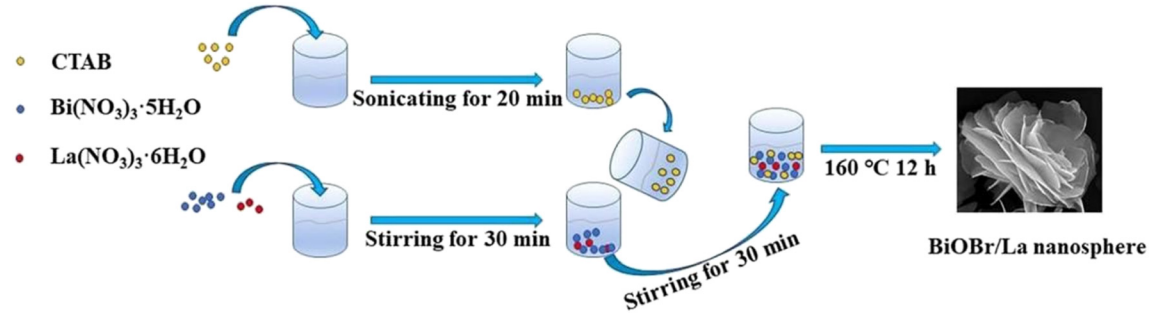


Fig. 16 Process diagram of BiOBr/La synthesis.[78]

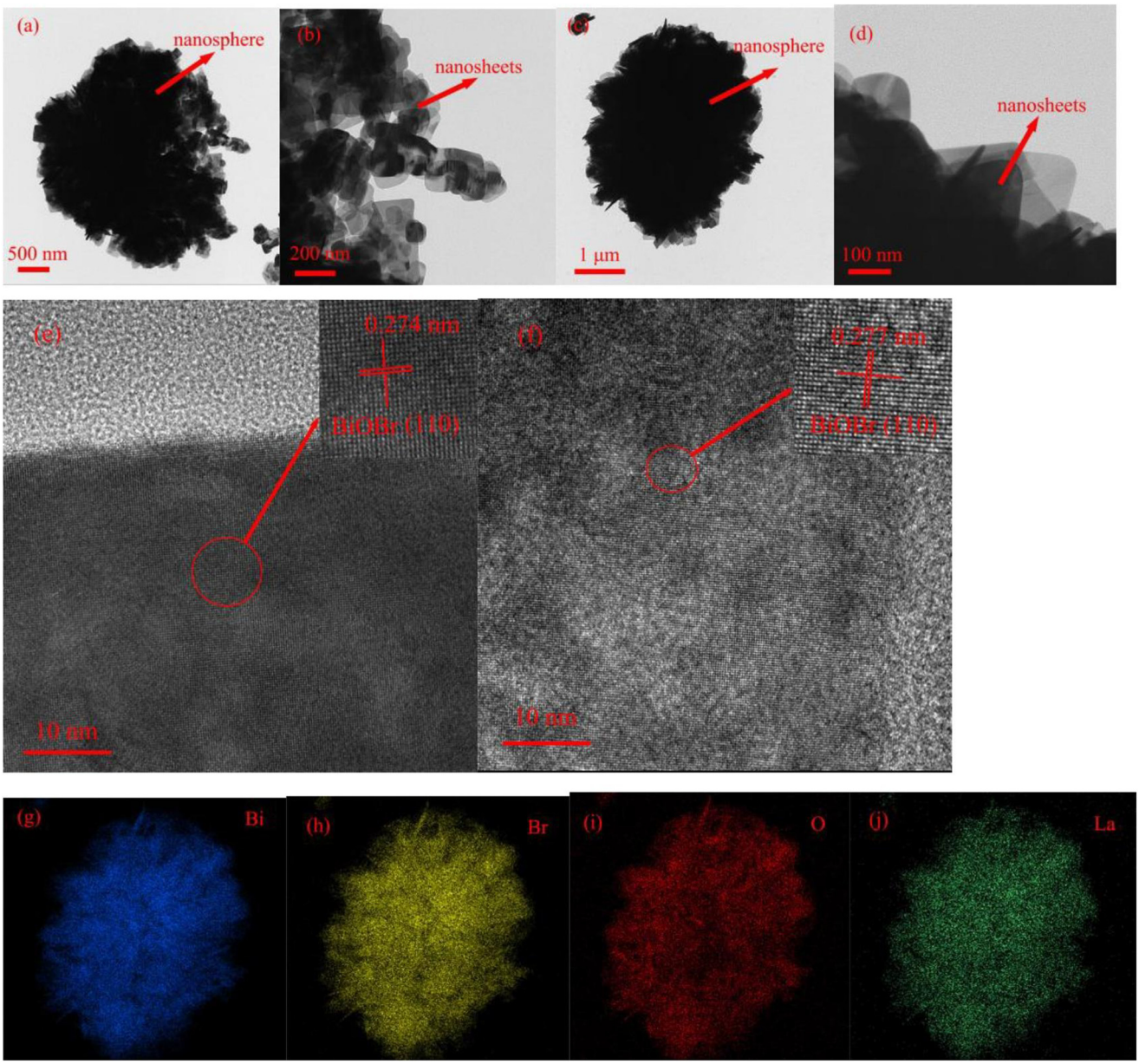


Fig. 17 TEM images of BiOBr (a and b), TEM images of BiOBr/La-4.9% (c and d), HRTEM images of BiOBr (e) and BiOBr/La-4.9% (f). EDX elements mapping images of Bi (g), Br (h), O (i), and La (j) in BiOBr/La-4.9%.[78]

 

directed to induce the enrichment of photogenerated electrons at the Pr monoatomic site under light thus significantly promoting the adsorption and activation of $CO_2$. Photocatalytic $CO_2$ reduction results show that, as shown in Fig. 15a, the $CH_3OH$ yield is significantly increased after the introduction of atomically dispersed $Pr_1$–$N_6$ and $Pr_1$–$N_4O_2$ active sites into CN. In addition, its $CH_3OH$ formation rate is higher than the CN loading of different kinds of metal monoatoms and other metal elements (Fig. 14e and f). However, in addition to $CH_3OH$, other by-products such as $H_2$, CO, $CH_4$ and $C_2H_4$ appear during $CO_2$ reduction (Fig. 3c). Nevertheless, it can be observed that the $CH_3OH$ selectivity on $Pr_1$–$N_4O_2$/CN is very high, reaching more than 90%. The experimental results of repeated use of $Pr_1$–$N_4O_2$/CN for 5 cycles (~20 h) to determine the durability of $Pr_1$–$N_4O_2$/CN showed that the yield and selectivity of $Pr_1$–$N_4O_2$/CN to $CH_3OH$ were very stable, and there was no obvious deactivation. This indicates that $Pr_1$–$N_4O_2$/CN has good durability for the synthesis of $CH_3OH$ by $CO_2$ photoreduction. In addition, Jiao *et al.*[78] developed novel flower-like La-doped BiOBr nanosheets, the synthesis process of which is schematically shown in Fig. 16. From the TEM imaging analysis, it can be seen that the structure is composed of nanospheres of nanosheets with uniform elemental distribution (Fig. 17). The results of its photoelectrochemical test analysis (Fig. 18) showed that due to the doping of $La^{3+}$, the photogenerated electrons located in the conduction band of BiOBr can be transferred to $La^{3+}$, which prolongs the lifetime and reduces the compounding rate, thus improving the photocatalytic performance. From the photocatalytic results (Fig. 19), we can find that the yield of $CH_3OH$ products for BiOBr/La-4.9% is much higher than that for the other groups after 3 h of irradiation. At the end of 5 cycles of experiments, the yield of $CH_3OH$ products can reach more than 90% of the first experiment, which indicates that BiOBr/La-4.9% has good chemical stability in the $CO_2$ reduction process. Comparison of the amount of each product shows that BiOBr/La-4.9% has a high selectivity for the generation of $CH_3OH$. The GC-MS

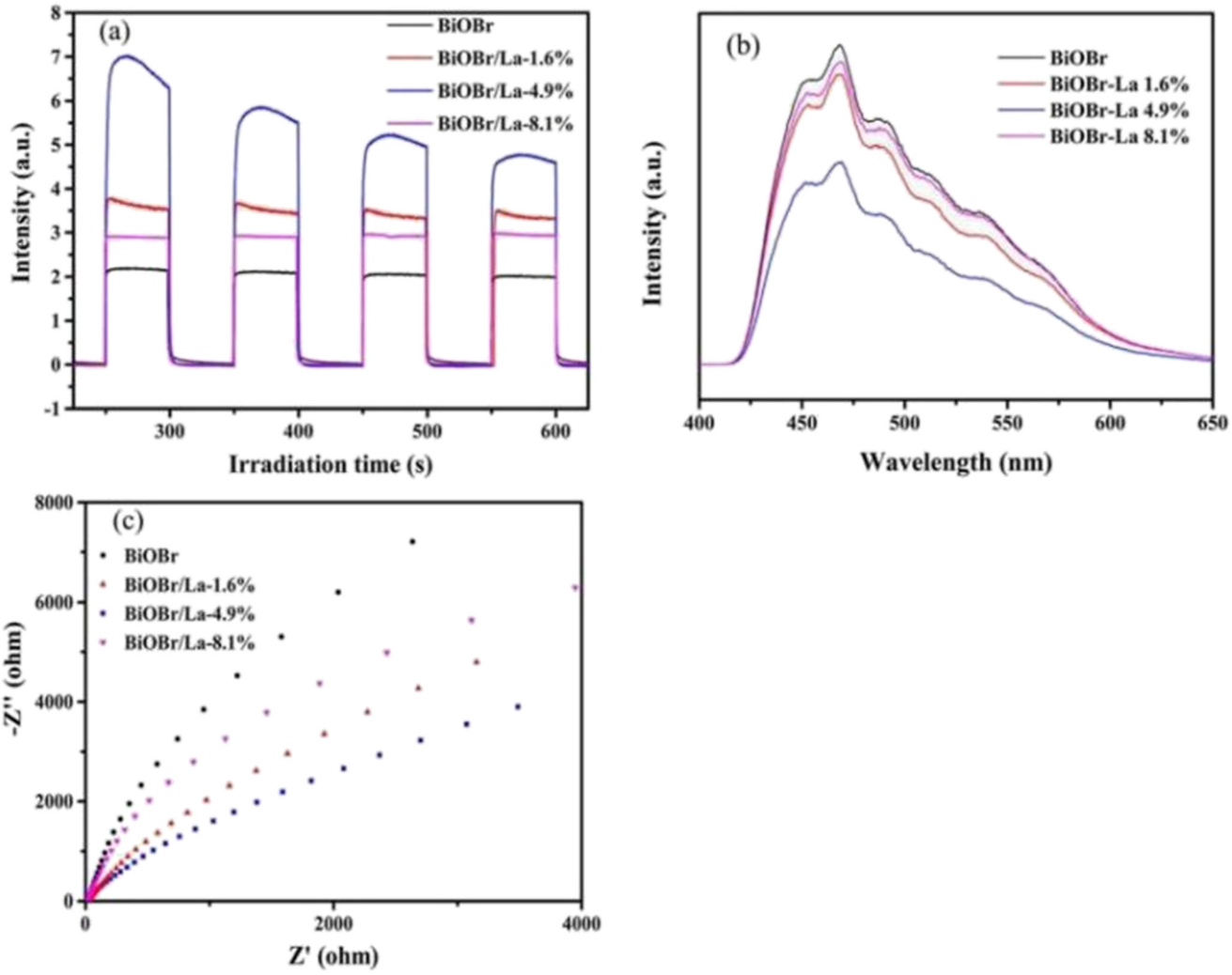


Fig. 18 Transient photocurrent curves (a), PL spectra (b), and EIS curves (c) for BiOBr and BiOBr/La catalysts.[78]

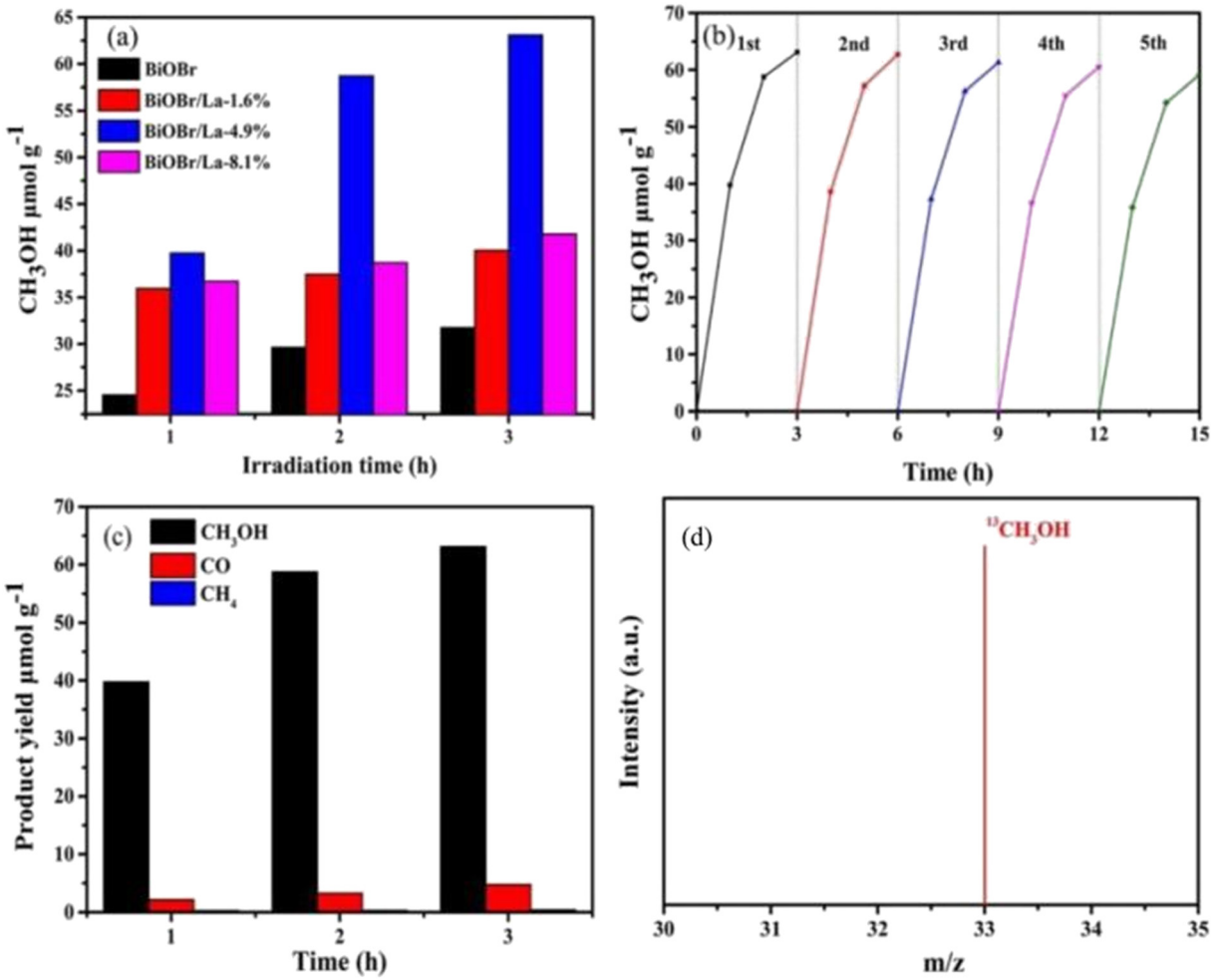


Fig. 19 (a) The yields of $CH_3OH$ for BiOBr and BiOBr/La catalysts, (b) cycling performance for BiOBr/La-4.9%, (c) products from $CO_2$ reduction on BiOBr/La-4.9% and (d) MS spectrum of $CH_3OH$ produced by $^{13}CO_2$ reduction.[78]

analysis in Fig. 19d is the reduction product of $^{13}CO_2$ photoreduction, where the strong signal in the MS spectrum at $m/z$ = 33 is $^{13}CH_3OH$. This result proves that $CO_2$ is the only carbon source of $CH_3OH$ reduction products.

In Table 3, we summarize the results of some studies on the reduction of $CO_2$ to $CH_3OH$ by single metal-doped photocatalysts. This kind of photocatalytic material mainly improves the photocatalytic performance of the original matrix material by loading metal atoms on the surface of the matrix material, thereby forming an active site on the surface of the matrix material and promoting charge transfer. At present, the methods for preparing such materials include pyrolysis,[77] solvent/hydrothermal,[78–81] acid-assisted,[82,83] sol–gel,[84,85] *etc.* The most commonly used method is the solvent/hydrothermal method, which is convenient and simple, and is also a common method for synthesizing other photocatalytic materials. From Table 3, we can also find that most of the single metal atoms used for doping belong to transition metals, because transition metals often contain d orbital electrons or empty d orbitals, which makes its d electron layer easy to lose electrons or seize electrons to form variable valence metal ions, which is conducive to the transfer of electron–hole pairs during photocatalytic reactions. Although single-metal doping has shown remarkable effect in improving the photocatalytic performance of the substrate materials, the transition metals used in it are often costly, and there are still problems of catalyst poisoning caused by improper use. Therefore, the development of green low-cost single metal-doped photocatalytic materials is worthy of further exploration by researchers.

### 3.6 Characteristics of different photocatalyst systems

Here, we can easily find a rich variety of photocatalytic systems used for photocatalytic reduction of $CO_2$ to $CH_3OH$, and different photocatalytic systems have their own characteristics. In Table 4, we briefly summarize the characteristics of the five photocatalytic systems mentioned in the paper, and it can be seen that no photocatalyst is perfect at present, and all of them have their own

 

Table 3 Reduction of $CO_2$ to $CH_3OH$ by different single metal-doped photocatalysts

| Photocatalysts | Reaction conditions | $CH_3OH$ yield | Ref. |
|---|---|---|---|
| $Pr_1$–$N_4O_2$/CN | Xenon lamp (300 W) | 511.1 μmol $g^{-1}$ $h^{-1}$ | 77 |
| La/BiOBr | Xenon lamp (300 W) | 22.77 μmol $g^{-1}$ $h^{-1}$ | 78 |
| Pt/ZnO | Continuous visible light (9 h) | 668 μmol $g^{-1}$ | 84 |
| Co/$TiO_2$/rGO | Xenon lamp (500 W) | 936 μmol $g_{cat}^{-1}$ | 86 |
| Co/ZnO/rGO | High pressure xenon lamp (400 W) | 30.1 μmol $g^{-1}$ | 85 |
| Pt/ZnO–ZnS | Xenon lamp (300 W) | 81.1 μmol $g^{-1}$ $h^{-1}$ | 87 |
| Ag NPs/ACFs | Xenon lamp (300 W) | 13.9 μmol $g^{-1}$ $h^{-1}$ | 82 |
| Ag–$Al_2O_3$ | UVC (200–280 nm) | 36.3 ppm | 79 |
| Cu/g-$C_3N_4$ | UV-visible xenon lamp (300 W) | 25.0 μmol $g^{-1}$ | 80 |
| $Pr^{3+}$/$La_{1-x}Pr_xMn_{0.6}Ni_{0.4}O_{3-\delta}$ | Visible light (300 °C) | 3.97 mmol $g^{-1}$ | 88 |
| Ti/$WO_3$ | — | 16.8 μmol $g^{-1}$ $h^{-1}$ | 83 |
| Cu/$SnS_2$ | Visible light ($\lambda \geq 420$ nm) | 0.99 μmol $g^{-1}$ $h^{-1}$ | 81 |

Table 4 Characteristics of different catalysts

| Photocatalysts | Traits | Limitations |
|---|---|---|
| LDH-based | Unique layered structure, interlayer cations can be selective | Rapid recombination of photogenerated charge carriers, low $CO_2$ adsorption activity, agglomerate easily |
| g-$C_3N_4$-based | Planar two-dimensional sheet structure, unique physical and chemical properties, safe and pollution-free | Small specific surface area, low visible light absorption power, rapid recombination of photogenerated charge carriers |
| GO-based | Single atomic layer structure, high stability, excellent electrical conductivity, multifunctional groups | High cost, difficult to synthesize, research immaturity |
| Mixed metal compound | Good electrical conductivity, appropriate bandgap width | Uniformity of materials, the dispersion of elements on the surface of materials is difficult to control |
| Single metal-doped | Highly active site, high selectivity, stability, easy separation | High surface energy, atoms easily aggregate |

shortcomings. In the future, when designing photocatalytic materials, not only their photocatalytic performance should be considered, but also the service life, atomic utilization, recyclability, *etc.* of the materials should be taken into account from the perspective of environmental protection. A single material as a photocatalyst has obviously exposed its shortcomings, so, combined with the characteristics of various materials, the development of new composite materials to achieve "1 + 1 > 2" performance improvement is a good choice.

## 4. Challenges and future prospects

In the context of global energy shortages, the production of solar fuels through the photocatalytic reduction of $CO_2$ presents a promising strategy to address environmental challenges and ensure future energy security. Methanol ($CH_3OH$), as a new type of clean energy fuel, has the potential to replace some fossil fuels and offers advantages in reducing energy consumption. Therefore, using photocatalytic processes to convert $CO_2$ into $CH_3OH$ holds great promise for addressing future energy needs.

Recent years have seen noted innovations in the development of nanocomposite photocatalysts designed to enhance the efficiency of $CO_2$ reduction to $CH_3OH$. A key advancement has been made in layered double hydroxide (LDH) photocatalysts, where the synergistic integration of metal cations within a single-layered structure improves charge separation and optimizes electronic properties, leading to more efficient $CO_2$ conversion. Similarly, significant improvements in graphitic carbon nitride (g-$C_3N_4$) photocatalysts have been achieved through structural modifications and element doping, which extend light absorption into the visible spectrum and enhance charge separation, thereby boosting the overall photocatalytic performance. Innovations in graphene oxide (GO)-based photocatalysts have also been noteworthy; their high surface area and exceptional electron conductivity have driven the development of GO-based composites. These composites combine GO with other materials, effectively reducing electron–hole recombination and increasing $CO_2$ adsorption, resulting in higher $CH_3OH$ yields. Collectively, these advancements, along with progress in mixed metal compounds and single metal-doped photocatalysts, underscore the potential for developing more effective and scalable solutions for $CO_2$ reduction, as they improve light absorption, enhance charge separation, and facilitate multi-electron transfer processes.

However, despite these advancements, challenges remain in the photocatalytic reduction process. These include competitive by-product reactions, limited light absorption, the recombination of photogenerated electron–hole pairs, low photocatalyst stability, and the need for improved $CO_2$ capture. To address these challenges, researchers have focused on enhancing photocatalyst performance by synthesizing binary or multivariate composites, metal doping,

and ligand displacement. Moving forward, it will be crucial to explore ways to further improve the selectivity to and yield of $CH_3OH$ in photocatalytic reactions by optimizing the process. Additionally, achieving large-scale mass production of $CH_3OH$ through photocatalytic $CO_2$ reduction remains a significant challenge that will require substantial attention and effort from the research community for sustainable long-term development.

## Data availability

No primary research results, software or code have been included and no new data were generated or analysed as part of this review.

## Conflicts of interest

There are no conflicts to declare.

## Acknowledgements

This project is supported by The Leverhulme Trust Early Career Fellowship funding under award number ECF-2021-657.

## References

1 Y. Chen, G. Jia and Y. Hu, *et al.*, Two-dimensional nanomaterials for photocatalytic $CO_2$ reduction to solar fuels, *Sustainable Energy Fuels*, 2017, **1**, 1875–1898.
2 H. Lin, S. Luo and H. Zhang, *et al.*, Toward solar-driven carbon recycling, *Joule*, 2022, **6**(2), 294–314.
3 Y. A. Ye, B. Rtga and A. Lfh, A review of metal oxide-based Z-scheme heterojunction photocatalysts: Actualities and developments, *Mater. Today Energy*, 2021, **21**, 100829.
4 Q. Xu, L. Zhang and B. Cheng, *et al.*, S-Scheme Heterojunction Photocatalyst, *Chem*, 2020, **6**(7), 1543–1559.
5 A. Mn, B. Vs and C. Tian, *et al.*, Recent advances in visible-light-driven carbon dioxide reduction by metal-organic frameworks, *Sci. Total Environ.*, 2020, **762**, 144101.
6 Z. Fu, Q. Yang, Z. Liu, F. Chen, F. Yao, T. Xie, Y. Zhong, D. Wang, J. Li, X. Li and G. Zeng, Photocatalytic conversion of carbon dioxide: From products to design the catalysts, *J. CO2 Util.*, 2019, **34**, 63–73.
7 K. Li, B. Peng and T. Peng, Recent Advances in Heterogeneous Photocatalytic $CO_2$ Conversion to Solar Fuels, *ACS Catal.*, 2016, 7485–7527.
8 J. Fu, K. Jiang and X. Qiu, *et al.*, Product selectivity of photocatalytic $CO_2$ reduction reactions, *Mater. Today*, 2019, **32**, 222–243.
9 X. Bian, S. Zhang and Y. Zhao, *et al.*, Layered double hydroxide-based photocatalytic materials toward renewable solar fuels production, *InfoMat*, 2021, **3**(7), 719–738.
10 Z. Bi, R. Guo and X. Hu, *et al.*, Research progress on photocatalytic reduction of $CO_2$ based on LDH materials, *Nanoscale*, 2022, **14**(9), 3367–3386.
11 C. G. Silva, Y. Bouizi and V. Fornés, *et al.*, Layered double hydroxides as highly efficient photocatalysts for visible light oxygen generation from water, *J. Am. Chem. Soc.*, 2009, **131**(38), 13833–13839.
12 K. Teramura, S. Iguchi and Y. Mizuno, *et al.*, Photocatalytic conversion of $CO_2$ in water over layered double hydroxides, *Angew. Chem., Int. Ed.*, 2012, **51**(32), 8008–8011.
13 A. Ziarati, A. Badiei and R. Grillo, *et al.*, 3D Yolk@ Shell $TiO_2$–x/LDH architecture: tailored structure for visible light $CO_2$ conversion, *ACS Appl. Mater. Interfaces*, 2019, **11**(6), 5903–5910.
14 L. Zhu, C. Qin, Y. Wang and J. Cao, Single-atom Pt supported on non-metal doped $WS_2$ for photocatalytic $CO_2$ reduction: A first-principles study, *Appl. Surf. Sci.*, 2023, **626**, 157252.
15 J.-C. Wang, N. Li, A. M. Idris, J. Wang, X. Du, Z. Pan and Z. Li, Surface Defect Engineering of $CsPbBr_3$ Nanocrystals for High Efficient Photocatalytic $CO_2$ Reduction, *Sol. RRL*, 2021, **5**(7), 2100154.
16 P. M. Stanley, K. Hemmer, M. Hegelmann, A. Schulz, M. Park, M. Elsner, M. Cokoja and J. Warnan, Topology- and wavelength-governed $CO_2$ reduction photocatalysis in molecular catalyst-metal-organic framework assemblies, *Chem. Sci.*, 2022, **13**(41), 12164–12174.
17 X. Zhang, K. Hu, X. Zhang, W. Ali, Z. Li, Y. Qu, H. Wang, Q. Zhang and L. Jing, Surface co-modification with highly-dispersed Mn & Cu oxides of g-$C_3N_4$ nanosheets for efficiently photocatalytic reduction of $CO_2$ to CO and $CH_4$, *Appl. Surf. Sci.*, 2019, **492**, 125–134.
18 D. Chen, Z. Wang, J. Zhang, O. Ruzimuradov, S. Mamatkulov, K. Dai and J. Low, Modulation of internal electric field in S-scheme heterojunction towards efficient photocatalytic $CO_2$ conversion, *Mater. Today Phys.*, 2024, **40**, 101315.
19 Y. Jiang, J. Guo and X. Li, *et al.*, Direct Z-scheme 0D/2D heterojunction of CuO quantum Dots/ultrathin CoAl-LDH for boosting charge separation and photocatalytic $CO_2$ reduction, *Sol. Energy*, 2022, **231**, 705–715.
20 J. Wen, J. Xie and X. Chen, *et al.*, A review on g-$C_3N_4$-based photocatalysts, *Appl. Surf. Sci.*, 2017, **391**, 72–123.
21 Z. Sun, H. Wang and Z. Wu, *et al.*, g-$C_3N_4$ based composite photocatalysts for photocatalytic $CO_2$ reduction, *Catal. Today*, 2018, **300**, 160–172.
22 X. Wang, K. Maeda and A. Thomas, *et al.*, A metal-free polymeric photocatalyst for hydrogen production from water under visible light, *Nat. Mater.*, 2009, **8**(1), 76–80.
23 A. Li, T. Wang and C. Li, *et al.*, Adjusting the reduction potential of electrons by quantum confinement for selective photoreduction of $CO_2$ to methanol, *Angew. Chem., Int. Ed.*, 2019, **58**(12), 3804–3808.
24 M. Liang, T. Borjigin and Y. Zhang, *et al.*, Controlled assemble of hollow heterostructured g-$C_3N_4$@ $CeO_2$ with rich oxygen vacancies for enhanced photocatalytic $CO_2$ reduction, *Appl. Catal., B*, 2019, **243**, 566–575.
25 N. Li, M. Huang and J. Zhou, *et al.*, MgO and Au nanoparticle Co-modified g-$C_3N_4$ photocatalysts for enhanced photoreduction of $CO_2$ with $H_2O$, *Chin. J. Catal.*, 2021, **42**(5), 781–794.

 

26 M. Ma, Z. Huang and R. Wang, *et al.*, Targeted $H_2O$ activation to manipulate the selective photocatalytic reduction of $CO_2$ to $CH_3OH$ over carbon nitride-supported cobalt sulfide, *Green Chem.*, 2022, **24**(22), 8791–8799.
27 J. Ding, Q. Tang and Y. Fu, *et al.*, Core–Shell Covalently Linked Graphitic Carbon Nitride–Melamine–Resorcinol–Formaldehyde Microsphere Polymers for Efficient Photocatalytic $CO_2$ Reduction to Methanol, *J. Am. Chem. Soc.*, 2022, **144**(22), 9576–9585.
28 W. Wang, S. Song and P. Wang, *et al.*, Chemical Bonding of g-$C_3N_4$/UiO-66 (Zr/Ce) from Zr and Ce Single Atoms for Efficient Photocatalytic Reduction of $CO_2$ under Visible Light, *ACS Catal.*, 2023, **13**(7), 4597–4610.
29 A. Bafaqeer, M. Tahir and A. Ali Khan, *et al.*, Indirect Z-scheme assembly of 2D $ZnV_2O_6$/RGO/g-$C_3N_4$ nanosheets with RGO/pCN as solid-state electron mediators toward visible-light-enhanced $CO_2$ reduction, *Ind. Eng. Chem. Res.*, 2019, **58**(20), 8612–8624.
30 Y. Huo, J. Zhang and K. Dai, *et al.*, All-solid-state artificial Z-scheme porous g-$C_3N_4$/$Sn_2S_3$-DETA heterostructure photocatalyst with enhanced performance in photocatalytic $CO_2$ reduction, *Appl. Catal., B*, 2019, **241**, 528–538.
31 H. Guo, J. Ding and S. Wan, *et al.*, Highly efficient $CH_3OH$ production over $Zn_{0.2}Cd_{0.8}S$ decorated g-$C_3N_4$ heterostructures for the photoreduction of $CO_2$, *Appl. Surf. Sci.*, 2020, **528**, 146943.
32 M. S. Akple, S. P. Chimmikuttanda and G. K. S. Takyi, *et al.*, Fabrication and density functional theory calculations of bromine doped carbon nitride nanosheets with enhanced photocatalytic reduction of $CO_2$ into solar fuels, *Biointerface Res. Appl. Chem.*, 2021, **11**, 14602–14619.
33 M. H. Foghani, O. Tavakoli and M. J. Parnian, *et al.*, Enhanced visible light photocatalytic $CO_2$ reduction over direct Z-scheme heterojunction Cu/P co-doped g-$C_3N_4$@ $TiO_2$ photocatalyst, *Chem. Pap.*, 2022, **76**(6), 3459–3469.
34 H. Guo, T. Zhang and W. Ma, *et al.*, Construction of sandwich-like Ag/UiO-66@ g-$C_3N_4$ Z-scheme ternary heterojunction for photocatalytic $CO_2$ conversion to $CH_3OH$ and CO, *Fuel*, 2023, **344**, 127911.
35 H. C. Hsu, I. Shown and H. Y. Wei, *et al.*, Graphene oxide as a promising photocatalyst for $CO_2$ to methanol conversion, *Nanoscale*, 2013, **5**(1), 262–268.
36 Y. Kuang, J. Shang and T. Zhu, Photoactivated graphene oxide to enhance photocatalytic reduction of $CO_2$, *ACS Appl. Mater. Interfaces*, 2019, **12**(3), 3580–3591.
37 T. F. Yeh, J. M. Syu and C. Cheng, *et al.*, Graphite oxide as a photocatalyst for hydrogen production from water, *Adv. Funct. Mater.*, 2010, **20**(14), 2255–2262.
38 Y. Shi, W. Su and L. Kong, *et al.*, The homojunction formed by h-$In_2O_3$ (1 1 0) and c-$In_2O_3$ (4 4 0) promotes carbon dioxide hydrogenation to methanol on graphene oxide modified $In_2O_3$, *J. Colloid Interface Sci.*, 2022, **623**, 1048–1062.
39 Y. Zhang, L. Zheng and J. Jia, *et al.*, Construction of 2D-coal-based graphene/2D-bismuth vanadate compound for effective photocatalytic $CO_2$ reduction to $CH_3OH$, *Colloids Surf., A*, 2022, **639**, 128321.
40 A. Bafaqeer, M. Tahir and A. Ali Khan, *et al.*, Indirect Z-scheme assembly of 2D $ZnV_2O_6$/RGO/g-$C_3N_4$ nanosheets with RGO/pCN as solid-state electron mediators toward visible-light-enhanced $CO_2$ reduction, *Ind. Eng. Chem. Res.*, 2019, **58**(20), 8612–8624.
41 M. Mgolombane, O. M. Bankole and E. E. Ferg, *et al.*, Construction of Co-doped $TiO_2$/rGO nanocomposites for high-performance photoreduction of $CO_2$ with $H_2O$: Comparison of theoretical binding energies and exploration of surface chemistry, *Mater. Chem. Phys.*, 2021, **268**, 124733.
42 A. Nosrati, S. Javanshir and F. Feyzi, *et al.*, Effective $CO_2$ Capture and Selective Photocatalytic Conversion into $CH_3OH$ by Hierarchical Nanostructured GO–$TiO_2$– $Ag_2O$ and GO–$TiO_2$–$Ag_2O$–Arg, *ACS Omega*, 2023, **8**, 3981–3991.
43 Y. Xia, B. Cheng and J. Fan, *et al.*, Near-infrared absorbing 2D/3D $ZnIn_2S_4$/N-doped graphene photocatalyst for highly efficient $CO_2$ capture and photocatalytic reduction, *Sci. China Mater.*, 2020, **63**(4), 552.
44 P. Kumar, H. P. Mungse and S. Cordier, *et al.*, Hexamolybdenum clusters supported on graphene oxide: Visible-light induced photocatalytic reduction of carbon dioxide into methanol, *Carbon*, 2015, **94**, 91–100.
45 W. Zhang, F. Dong and W. Zhang, Capture of atmospheric $CO_2$ into $(BiO)_2CO_3$/graphene or graphene oxide nanocomposites with enhanced photocatalytic performance, *Appl. Surf. Sci.*, 2015, **358**, 75–83.
46 Y. Y. Lee, H. S. Jung and Y. T. Kang, A review: Effect of nanostructures on photocatalytic $CO_2$ conversion over metal oxides and compound semiconductors, *J. CO2 Util.*, 2017, **20**, 163–177.
47 M. Aggarwal, N. P. Shetti and S. Basu, *et al.*, Two-dimensional ultrathin metal-based nanosheets for photocatalytic $CO_2$ conversion to solar fuels, *J. Environ. Manage.*, 2022, **313**, 114916.
48 A. Fujishima and K. Honda, Electrochemical photolysis of water at a semiconductor electrode, *Nature*, 1972, **238**(5358), 37–38.
49 C. Ray and T. Pal, Retracted Article: Recent advances of metal–metal oxide nanocomposites and their tailored nanostructures in numerous catalytic applications, *J. Mater. Chem. A*, 2017, **5**(20), 9465–9487.
50 Z.-W. Huang, K.-Q. Hu, L. Mei, D.-G. Wang, J.-Y. Wang, W.-S. Wu, Z.-F. Chai and W.-Q. Shi, Encapsulation of Polymetallic Oxygen Clusters in a Mesoporous/Microporous Thorium-Based Porphyrin Metal–Organic Framework for Enhanced Photocatalytic $CO_2$ Reduction, *Inorg. Chem.*, 2022, **61**(8), 3368–3373.
51 Z.-W. Huang, K.-Q. Hu, X.-B. Li, Z.-N. Bin, Q.-Y. Wu, Z.-H. Zhang, Z.-J. Guo, W.-S. Wu, Z.-F. Chai and L. Mei, *et al.*, Thermally Induced Orderly Alignment of Porphyrin Photoactive Motifs in Metal–Organic Frameworks for Boosting Photocatalytic $CO_2$ Reduction, *J. Am. Chem. Soc.*, 2023, **145**(32), 18148–18159.
52 X. Wang, Y. Wang and M. Gao, *et al.*, $BiVO_4$/$Bi_4Ti_3O_{12}$ heterojunction enabling efficient photocatalytic reduction of

$CO_2$ with $H_2O$ to $CH_3OH$ and CO, *Appl. Catal., B*, 2020, **270**, 118876.

53 Q. Wang, Y. Zhou and K. Zhang, *et al.*, Defect-enrichment in porous interface of ultrathin CuO nanobelts realizes a novel $CO_2$ photoreduction pathway, *J. Mater. Chem. A*, 2023, **11**, 8776–8782.

54 J. Li, W. Pan and Q. Liu, *et al.*, Interfacial engineering of $Bi_{19}Br_3S_{27}$ nanowires promotes metallic photocatalytic $CO_2$ reduction activity under near-infrared light irradiation, *J. Am. Chem. Soc.*, 2021, **143**(17), 6551–6559.

55 X. Wu, Y. Li and G. Zhang, *et al.*, Photocatalytic $CO_2$ conversion of $M_{0.33}WO_3$ directly from the air with high selectivity: insight into full spectrum-induced reaction mechanism, *J. Am. Chem. Soc.*, 2019, **141**(13), 5267–5274.

56 C. Yang, Q. Li and Y. Xia, *et al.*, Enhanced visible-light photocatalytic $CO_2$ reduction performance of $Znln_2S_4$ microspheres by using $CeO_2$ as cocatalyst, *Appl. Surf. Sci.*, 2019, **464**, 388–395.

57 C. Luo, T. Yang and Q. Huang, *et al.*, CuMoxW (1-x) $O_4$ Solid Solution Display Visible Light Photoreduction of $CO_2$ to $CH_3$-OH Coupling with Oxidation of Amine to Imine, *Nanomaterials*, 2020, **10**(7), 1303.

58 E. Luévano-Hipólito and L. M. Torres-Martínez, $CO_2$ photoreduction with $H_2O$ to C1 and C2 products over perovskite films of alkaline niobates $ANbO_3$ (A= Li, Na, K), *Fuel*, 2022, **320**, 123934.

59 M. A. Ávila-López, E. Luévano-Hipólito and L. M. Torres-Martínez, $CO_2$ adsorption and its visible-light-driven reduction using CuO synthesized by an eco-friendly sonochemical method, *J. Photochem. Photobiol., A*, 2019, **382**, 111933.

60 K. Wang, Y. Du and Y. Li, *et al.*, Atomic-level insight of sulfidation-engineered Aurivillius-related $Bi_2O_2SiO_3$ nanosheets enabling visible light low-concentration $CO_2$ conversion, *Carbon Energy*, 2023, **5**(2), e264.

61 A. Hezam, K. Namratha and Q. A. Drmosh, *et al.*, $CeO_2$ nanostructures enriched with oxygen vacancies for photocatalytic $CO_2$ reduction, *ACS Appl. Nano Mater.*, 2019, **3**(1), 138–148.

62 W. Zhao, M. Ding and P. Yang, *et al.*, Pit-embellished low-valent metal active sites customize $CO_2$ photoreduction to methanol, *EES Catal.*, 2023, **1**, 36–44.

63 J. Albo and G. García, Enhanced visible-light photoreduction of $CO_2$ to methanol over $Mo_2C/TiO_2$ surfaces in an optofluidic microreactor, *React. Chem. Eng.*, 2021, **6**(2), 304–312.

64 J. Lu, Z. Zhang and L. Cheng, *et al.*, $MoS_2$-wrapped $Mn_{0.2}Cd_{0.8}S$ nanospheres towards efficient photocatalytic $H_2$ generation and $CO_2$ reduction, *New J. Chem.*, 2020, **44**(32), 13728–13737.

65 K. Zheng, Y. Wu and J. Zhu, *et al.*, Room-temperature photooxidation of $CH_4$ to $CH_3OH$ with nearly 100% selectivity over hetero-ZnO/$Fe_2O_3$ porous nanosheets, *J. Am. Chem. Soc.*, 2022, **144**(27), 12357–12366.

66 M. Flores-Flores, E. Luévano-Hipólito and L. M. Torres-Martínez, *et al.*, $CO_2$ adsorption and photocatalytic reduction over Mg $(OH)_2$/CuO/$Cu_2O$ under UV-Visible light to solar fuels, *Mater. Chem. Phys.*, 2019, **227**, 90–97.

67 M. Tahir, Hierarchical 3D $VO_2/ZnV_2O_4$ microspheres as an excellent visible light photocatalyst for $CO_2$ reduction to solar fuels, *Appl. Surf. Sci.*, 2019, **467**, 1170–1180.

68 Z. H. He, C. S. Jiang and K. Wang, *et al.*, Photothermal $CO_2$ hydrogenation to methanol over a CoO/Co/$TiO_2$ catalyst in aqueous media under atmospheric pressure, *Catal. Today*, 2020, **356**, 579–588.

69 Z. Luo, Y. Li and F. Guo, *et al.*, Carbon dioxide conversion with high-performance photocatalysis into methanol on $NiSe_2/WSe_2$, *Energies*, 2020, **13**(17), 4330.

70 S. P. Cheng, L. W. Wei and H. P. Wang, Photocatalytic reduction of $CO_2$ to methanol by $Cu_2O/TiO_2$ heterojunctions, *Sustainability*, 2021, **14**(1), 374.

71 M. A. Ávila-López, E. Luévano-Hipólito and L. M. Torres-Martínez, Optimizing the $CO_2$ reduction to produce $CH_3OH$ using flexible $NiMoO_4$ coatings as a photocatalyst, *J. Alloys Compd.*, 2022, **918**, 165549.

72 W. Cai, X. Yu and Y. Cao, *et al.*, Electron-coupled enhanced interfacial interaction of Ce-MOF/$Bi_2MoO_6$ heterostructure for boosted photoreduction $CO_2$, *J. Environ. Chem. Eng.*, 2022, **10**(3), 107461.

73 Y. Liu, X. Chu and A. Shi, *et al.*, Construction of 2D Bismuth Silicate Heterojunctions from Natural Mineral toward Cost-Effective Photocatalytic Reduction of $CO_2$, *Ind. Eng. Chem. Res.*, 2022, **61**(34), 12294–12306.

74 K. A. Alzahrani, A. A. Ismail and N. Alahmadi, $CuCo_2O_4$/$CeO_2$ S-scheme photocatalyst for promoted $CO_2$ photoreduction to $CH_3OH$, *J. Mol. Liq.*, 2023, **376**, 121509.

75 S. Wang, H. Abroshan and C. Liu, *et al.*, Shuttling single metal atom into and out of a metal nanoparticle, *Nat. Commun.*, 2017, **8**(1), 848.

76 J. Xing, J. F. Chen and Y. H. Li, *et al.*, Stable isolated metal atoms as active sites for photocatalytic hydrogen evolution, *Chem. – Eur. J.*, 2014, **20**(8), 2138–2144.

77 M. Ma, Z. Huang and L. Li, *et al.*, Modulating photogenerated electron density of Pr single-atom sites by coordination environment engineering for boosting photoreduction of $CO_2$ to $CH_3OH$, *Appl. Catal., B*, 2023, **330**, 122626.

78 W. Jiao, Y. Xie and F. He, *et al.*, A visible light-response flower-like La-doped BiOBr nanosheets with enhanced performance for photoreducing $CO_2$ to $CH_3OH$, *Chem. Eng. J.*, 2021, **418**, 129286.

79 H. J. Yoon, J. H. Yang and S. J. Park, *et al.*, Thermal CO oxidation and photocatalytic $CO_2$ reduction over bare and M-$Al_2O_3$ (M= Co, Ni, Cu, Rh, Pd, Ag, Ir, Pt, and Au) cotton-like nanosheets, *Nanomaterials*, 2021, **11**(5), 1278.

80 H. Du, X. Gao and Q. Ma, *et al.*, Cu/PCN Metal-Semiconductor Heterojunction by Thermal Reduction for Photoreaction of $CO_2$-Aerated $H_2O$ to $CH_3OH$ and $C_2H_5OH$, *ACS Omega*, 2022, **7**(19), 16817–16826.

81 T. Di, T. Cao and H. Liu, *et al.*, Cu doped $SnS_2$ nanosheets with superior visible-light photocatalytic $CO_2$ reduction performance, *Phys. Chem. Chem. Phys.*, 2023, **25**, 5196–5202.

 

82 R. Wang, J. Ding and Q. Zhong, *et al.*, Plasmonic Ag nanoparticles decorated acid-aching carbon fibers for enhanced photocatalytic reduction of $CO_2$ into $CH_3OH$ under visible-light irradiation, *Catal. Lett.*, 2021, 1–10.

83 P. Ling, J. Zhu and Z. Wang, *et al.*, Ultrathin Ti-doped $WO_3$ nanosheets realizing selective photoreduction of $CO_2$ to $CH_3$-OH, *Nanoscale*, 2022, **14**(38), 14023–14028.

84 S. M. Albukhari and A. A. Ismail, Highly dispersed Pt nanoparticle-doped mesoporous ZnO photocatalysts for promoting photoconversion of $CO_2$ to methanol, *ACS Omega*, 2021, **6**(36), 23378–23388.

85 M. Mgolombane, S. Majodina and O. M. Bankole, *et al.*, Influence of surface modification of zinc oxide–based nanomaterials on the photocatalytic reduction of carbon dioxide, *Mater. Today Chem.*, 2021, **20**, 100446.

86 M. Mgolombane, O. M. Bankole and E. E. Ferg, *et al.*, Construction of Co-doped $TiO_2$/rGO nanocomposites for high-performance photoreduction of $CO_2$ with $H_2O$: Comparison of theoretical binding energies and exploration of surface chemistry, *Mater. Chem. Phys.*, 2021, **268**, 124733.

87 R. M. Mohamed, I. A. Mkhalid and M. Alhaddad, *et al.*, Enhanced $CO_2$ photocatalytic conversion into $CH_3OH$ over visible-light-driven Pt nanoparticle-decorated mesoporous ZnO–ZnS S-scheme heterostructures, *Ceram. Int.*, 2021, **47**(19), 26779–26788.

88 R. Han, L. Chen and B. Xing, *et al.*, $Pr^{3+}$-doped $La_{1-x}Pr_xMn_{0.6}Ni_{0.4}O_{3-\delta}$ as efficient artificial photosynthesis catalysts for solar methanol, *Catal. Commun.*, 2022, **165**, 106440.